# A level-set based continuous scanning path optimization method for reducing residual stress and deformation in metal additive manufacturing

Qian Chen, Jikai Liu, Xuan Liang, and Albert. C. To*

Department of Mechanical Engineering and Materials Science, University of Pittsburgh, Pittsburgh, Pennsylvania 15261, USA

*Corresponding author. Email: albertto@pitt.edu

## Abstract

Thermal residual stress and distortion inherent in metal melting and solidification process is the main cause of build failure in metal additive manufacturing (AM) techniques such as laser powder bed fusion and directed energy deposition. To ensure build quality against residual stress/distortion, it is desirable to tailor the scanning path for a given geometry that needs to be built. Since the local deformation introduced by the moving heat source is anisotropic due to non-uniform heat transfer and mechanical constraints, the scanning path can affect residual stress within a part significantly. Aiming at thermal residual stress/distortion mitigation, this paper presents a novel level set-based scanning path optimization method. The method is developed to enable layer-wise continuous scanning path optimization for geometrically well-defined parts. To make the optimization efficient, a fast process simulation method called the inherent strain method is employed to simulate the thermal residual strain. Full sensitivity analysis for the formulated compliance- and stress-minimization problems is provided, where a novel strategy called the adaptive level set adjustment (ALSA) is proposed to remedy the deficiency of ignoring the non-implementable sensitivity terms. The effectiveness of the proposed continuous scanning path optimization method and ALSA strategy has been proved by numerical examples. Finally, the concurrent design scenario for simultaneous scanning path and structural optimization is investigated to demonstrate the further residual stress reduction.

*Keywords:* continuous scanning path; level set method; residual stress mitigation; adaptive level set adjustment; concurrent design

## 1. Introduction

Metal additive manufacturing (AM) approaches, such as powder bed fusion (PBF), wire-feed additive manufacturing and directed energy deposition (DED) have emerged as the mainstream AM processes for metallic part fabrication. Among these approaches, the PBF process, including selective laser melting (SLM), electron beam melting (EBM) and directed metal laser sintering (DMLS), has the highest manufacturing accuracy and best surface finish. With this technique, metal powders are spread to form a thin material layer of tens of microns, and laser beam selectively melts the powders based on the geometric input. Once the layer-wise scanning is

finished, the build tray moves downwards to process the next layer. In directed energy deposition (DED) and wire-feed additive manufacturing, metal powder or wire is fed into the melt pool created by the heat source such as a laser, arc or electron beam. Compared with PBF, these approaches could build metal parts in much larger scale efficiently. These layer-by-layer fabrication processes can easily be utilized to fabricate complex geometries so that the potential to design higher performing structures for AM can be fully exploited. On the other hand, residual stress is inherent in these AM processes due to sharp thermal gradient and rapid cooling rate, which may lead to severe part distortion, cracking, and delamination from the build plate. This type of thermal stress-induced failure will cause a build to stop abruptly and thus will increase manufacturing time and cost.

To address this issue, the effect of scanning strategy on residual stress has been extensively investigated. Scanning strategy can be divided into two parts, namely the scanning parameters (heat source power and velocity, hatching space and layer thickness) and scanning path. Studies on scanning parameters in SLM have been performed to improve fabrication quality of parts with horizontal structures [1] and downfacing structures [2]. Studies on scanning path were mainly focused on the so-called island-type scanning pattern, in which the layer is divided into blocks and scanning is conducted in a block-by-block sequence. Different scanning orientations and island sizes have been explored to examine the influence on thermal residual stress [3-9]. Rather than focusing on the island scanning strategy effects, we will explore free-form continuous scanning path optimization on residual stress mitigation for metal parts. The continuous scanning strategy is a scanning pattern with high efficiency widely used for different metal AM processes, including PBF, wire-feed additive manufacturing [10] and DED process [11]. Ding et al [12, 13] proposed a continuous path planning method based on medial axis transformation algorithm to produce void- and gap-free part in wire + arc additive manufacturing (WAAM). To the best of the authors' knowledge, optimizing continuous scanning path for residual stress reduction has not been studied yet. The main obstacles include complexity of the optimization problem and computational expense of full scale AM process simulation.

Even though continuous scanning path optimization for metal additive manufacturing has never been tackled, there are extensive numerical studies on optimal path planning on fiber reinforcement design or polymer AM, wherein material properties are greatly affected by build path orientation. Ponche [14] proposed a global design for AM (DfAM) framework to consecutively design the build direction, structural shape, and deposition paths. Hoglund [15] performed compliance minimization topology optimization with fiber angles as additional design variables for fiber-reinforced polymer printing. A limitation of this method is that fiber angles are treated as discrete variables without considering the overall printing path smoothness and continuity. To address this issue, filters [16-18] are introduced to project the discrete angle variables for smoothness improvement. Other than that, a level set-based continuous fiber path optimization method was proposed by Brampton et al [19]. Fiber paths were defined by iso-value

level set contours, so that continuity is always guaranteed. Beyond that, smoothness of the paths can be addressed by adding curvature constraints, and signed distance property of the level set field makes it trivial to derive a ready-to-print deposition path. However, there are also limitations of this method that the solution is heavily dependent on the initial guess and convergence is reported to be slow. Another level set-based continuous path optimization method was developed by Liu et al [20], wherein the structural topology was concurrently optimized rather than fixing the structural geometry. With that method, deposition path planning is performed by offsetting the structural boundary, and hence it cannot handle deposition path optimization for fixed geometry. In addition to fiber deposition and polymer printing, the level set method has been applied to contour-offset path generation for traditional machining [21, 22] as well.

Among the aforementioned methods, the approach developed in [19] will be referred in this work since similar continuous path optimization problem for well-defined geometry is the subject of interest here. Improvements will be made to this approach to enhance the robustness and convergence speed. More importantly, 3D stress minimization problem will be solved in addition to compliance minimization. Beyond that, part of the sensitivity (in domain integration form) was ignored in their implementation [19]. That may be fine for compliance-type problems, but may cause severe convergence fluctuations or divergence for stress minimization problem. Therefore, we have proposed the adaptive level set adjustment (ALSA) strategy to remedy the negative impact of ignoring part of the sensitivity result. Another major difference is that the underlying physics are different. Unlike polymer printing in which the process-induced material anisotropy is inevitable, material anisotropy of metals is much less significant [23], which often times can just be ignored. Therefore, the effect of scanning path on material constitutive model is ignored in the proposed optimization model, while the thermal residual strain is assumed to be dependent on the scanning path [24]. More details about these physics will be illustrated in Section 2.

As discussed earlier, the high computational expense of full scale process simulation is another obstacle toward implementing scanning path optimization. In general, full-scale process simulation for metal AM takes hours or days for a typical part. Therefore, it is impractical to implement detailed full-scale simulation based scanning path optimization, since it may require hundreds of iterations to converge. This challenge has drawn quite some attention, and many fast simulation models have been proposed recently. In this research, the recently proposed modified inherent strain method [24, 25] is adopted for its fast speed and acceptable prediction accuracy. Details about the modified inherent strain method will be discussed in Section 2, and briefly speaking, the inherent strain-based fast prediction can shorten the simulation time to minutes with good accuracy, e.g., usually less than 10% error for residual deformation.

In summary, existing optimization methods have partially addressed the deposition path planning in terms of 2D compliance cases and discontinuous elemental angle optimization but it

still deserves more exploration to advance the state-of-the-art. This paper is organized as follows: In Section 2, the modified inherent strain method, a novel method for part-scale stress and distortion simulation of the metal AM process, is presented. Section 3 presents the level set based formulation of compliance and stress minimization. Section 4 details the adaptive level set adjustment and, the numerical strategy developed for effective contour update and convergence. The effectiveness of this continuous deposition optimization framework is demonstrated by several 3D numerical examples in Section 5. Section 6 presents the extension of the proposed method to concurrent design to address the structure and scanning path simultaneously. In Section 7, discussions and conclusions are given.

## 2. Modified inherent strain method

Although the mechanism of residual stress and distortion in laser powder AM process has been extensively studied through numerical simulations in micro-scale [5, 26-28], there is still a large gap between these finite element models and part scale AM part prediction. For example, a full-scale thermomechanical simulation for a large EBM part consisting of 107 layers takes 15 hours to complete by running the Pan Computing software [29], which is one of the fastest commercial software packages with well-developed numerical techniques. Because of the high computational expense, full-scale simulation for metal AM part residual distortion and stress prediction is impractical, particularly for gradient-based iterative optimization.

To address this issue, the inherent strain method is adopted as an alternative solution. The inherent strain method was originally introduced by Ueda to simulate conventional welding decades ago [30]. The basic theory of this method is that residual distortion and stress are the result of incompatible internal strains, such as plastic, elastic and phase transformation strains. After the welding is completed, elastic strain is fully relaxed and thus the inherent strain equals the plastic strain generated in the welding process [31-34].

Unlike welding problems that only have single or a few welds, a metal part produced by AM utilizing a high energy source consists of thousands of layers and also thousands of scan lines in each layer. Boundary conditions in the process simulation dynamically evolve in a thermomechanical analysis. Hence, elastic strains due to thermal expansion mismatch cannot be fully released as in welding problems. Considering this new phenomenon in AM, Liang et al [24, 35] proposed a modified inherent strain model to predict residual stress and distortion at the part scale. The proposed model allows for extraction of accurate inherent strains directly from results of high-fidelity microscale detailed process simulation by solving the transient thermomechanical problem. As shown in these previous works, the inherent strains are anisotropic with respect to the scanning direction due to the non-uniform heat transfer caused by the moving heat source. In general, the inherent strain along the scan direction is compressive with the largest amplitude among the three normal strain components. The inherent strain transverse to the scan direction is also compressive but with a smaller amplitude, while that in the build direction is tensile due to the Poisson effect. This scanning orientation dependency in

the inherent strains is the reason why changing the scanning path in the AM process has a significant effect on the residual stress and strain distribution.

After the scanning orientation-dependent inherent strains are computed from the elastic and plastic strain histories obtained, they are being treated as thermal strains on the AM part in a series of layer-by-layer static equilibrium analysis. To carry out the inherent strain based analysis in commercial finite element software, the scanning orientation-dependent thermal strains are inputted as the thermal expansion coefficients, and a unit temperature rise is applied to carry out the analysis. Due to its high efficiency, inherent strain based AM process simulation has drawn increasing attention from academia [36-38] and industry. Most of the commercial AM process simulation packages, such as Simufact (MSC), Amphyon, Pan Computing (AutoDesk) and 3DSim (ANSYS), have adopted the inherent strain method in their software. Unfortunately, as these software packages are proprietary, the detailed theory and algorithm employed in the software packages are not available to the general public.

In this paper, scanning orientation-dependent inherent strain vector based on Ref. [25] is employed to approximate the thermal loading introduced in the metal AM process. In every iteration step, the nodal load vector of an element is given as:

$$\mathbf{f_e^{th}} = \int_{\Omega_e} \mathbf{B_e^T} \cdot \mathbf{C_e} \cdot \boldsymbol{\varepsilon}^{\mathbf{in}}(\theta_e)\Delta T \mathrm{d}\Omega \tag{1}$$

where $\mathbf{f_e^{th}}$ is the nodal vector of element $e$, $\mathbf{B_e^T}$ is the strain-displacement matrix, $\mathbf{C_e}$ is the element elasticity matrix, $\boldsymbol{\varepsilon}^{\mathbf{in}}(\theta_e)$ is the inherent strain vector as a function of the element scanning orientation $\theta_e$, which can be obtained from the level set function. By rotating the local inherent strain vector, the inherent strains in the global coordinate system corresponding to different scanning angle can be computed.

## 3. Continuous scanning path optimization formulation

### 3.1 Level set scanning path

The level set method is a mathematical framework developed by Osher and Sethian for implicit moving interface analysis and tracking [39]. This implicit representation can easily find if a point is inside or outside the boundary profile, and is a powerful tool for any physics-driven boundary evolution problem. Wang et al [40] and Allaire et al [41] developed the structural topology optimization method with level set method, which has the advantages of clear-cut interface representation and accessible high-order boundary information. As a mainstream topology optimization method, level set method has further successful applications for complex design problems, such as multi-material design [42-45], manufacturing cost [46] and feature insertion [47, 48].

Here, we focus on evolving the continuous scanning paths with level set method subject to a pre-defined part geometry, and hence, the problem formulation is similar to that for topology optimization. Beyond scanning path optimization, concurrent design that optimizes structure and

scanning path simultaneously will be explored in Section 6. Therefore, we will have the design domain ($D$) and material domain ($\Omega$) definitions in the problem formulation for consistency, even though the part geometry would not change when only optimizing scanning path. The level set function is defined by Eq. (2) to interpolate the design domain. A positive level set value indicates solid domain, negative value represents void, and zero-value contour represents a boundary:

$$\begin{cases} \Phi(\mathbf{X}) > 0, & \mathbf{X} \in \Omega/\partial\Omega \\ \Phi(\mathbf{X}) = 0, & \mathbf{X} \in \partial\Omega \\ \Phi(\mathbf{X}) < 0, & \mathbf{X} \in D/\Omega \end{cases} \tag{2}$$

Then, the part will be sliced into $N$ layers, each of which is coupled with one level set function for scanning path and another for the well-defined geometry:

$$\mathbf{\Phi^{scan}} = [\phi^{scan,1} \quad \phi^{scan,2} \quad \cdots \quad \phi^{scan,n}] \tag{3}$$

$$\mathbf{\Phi^{geo}} = [\phi^{geo,1} \quad \phi^{geo,2} \quad \cdots \quad \phi^{geo,n}] \tag{4}$$

Then, scanning path profile update will be identical to that in level set topology optimization. Updating velocities are derived from sensitivity analysis and the scanning paths are updated by solving the Hamilton-Jacobi equation through the standard up-wind scheme:

$$\phi_t + V_N|\nabla\phi| = 0 \tag{5}$$

where $V_N$ is the boundary velocity along the normal direction.

Beyond continuity, another advantage of using level set method for scanning path optimization is that $\phi^{scan,k}$ is a signed distance function ($|\nabla\phi| = 1$), so that scanning paths can be trivially obtained by extracting iso-value level set contours. A constant interval value will be employed between any pair of adjacent level set contours, and this value would just be set equal to the hatch spacing for the laser scanning paths. Therefore, reinitialization is incorporated in each iteration step to keep the signed distance property. The reinitialization is performed through fast marching method proposed by Sethian [49, 50], as shown below:

$$\phi_t + S(\phi) \cdot (\nabla\phi - 1) = 0 \tag{6}$$

where $S(\phi)$ is a sign function taken as 1 when $\phi > 0$, -1 when $\phi < 0$, and 0 on the boundary. In the fast marching method, it is formulated as:

$$S(\phi) = \frac{\phi}{\sqrt{\phi^2 + |\nabla\phi|^2 \Delta x}} \tag{7}$$

### 3.2 Compliance minimization

In this sub-section, thermomechanical loading induced by laser melting will be modified through laser scanning path optimization for stiffness improvement, i.e. reducing compliance and residual deformation by optimizing the scanning paths. The problem is formulated as below:

$$min. \quad J = \sum_{k=1}^{N} \left[ \int_{D_k} \mathbf{D_k e(u_k) e(u_k)} H(\phi^{geo,k}) d\Omega \right] \tag{8}$$

$$s.t.\, a(\mathbf{u}, \mathbf{v}, \boldsymbol{\Phi}^{\mathbf{geo}}) = l(\mathbf{v}, \boldsymbol{\Phi}^{\mathbf{geo}}), \quad \forall \mathbf{v} \in \mathbf{U_{ad}}$$

$$where.\ a(\mathbf{u}, \mathbf{v}, \boldsymbol{\Phi}^{\mathbf{geo}}) = \sum_{k=1}^{N} \int_{D_k} \mathbf{D_k e}(\mathbf{u_k}) \mathbf{e}(\mathbf{v_k})\, H(\phi^{geo,k}) d\Omega$$

$$l(\mathbf{v}, \boldsymbol{\Phi}^{\mathbf{geo}}) = \sum_{k=1}^{N} \int_{D_k} \mathbf{D_k e}\left(\mathbf{u^{in}}(\boldsymbol{\theta}^{\mathbf{k}})\right) \mathbf{e}(\mathbf{v_k})\, H(\phi^{geo,k}) d\Omega$$

where $\mathbf{u_k}$ and $\mathbf{v_k}$ are the deformation vector and test vector of the $k^{th}$ building layer, $\boldsymbol{\theta}^{\mathbf{k}}$ is the scanning orientation vector of $k^{th}$ building layer and $\mathbf{e}\left(\mathbf{u^{in}}(\boldsymbol{\theta}^{\mathbf{k}})\right)$ is the deposition orientation-dependent inherent strain vector. In this formulation, each printing layer is defined by a single level set function, and we assume $N$ layers in total are involved. Next, the geometry is defined by $\Phi^{geo}$ and the Heaviside function is used to project the material domain. Here, $\Phi^{geo}$ is involved in this problem formulation for potential extension to concurrent design problems (simultaneous design of scanning path and part geometry). Note that, each level set function can represent a group of consecutive deposition layers in order to reduce computational expense, but the tradeoff is that the inter-layer scanning effect on inherent strain between deposition layers within the group is not taken into account.

To solve this optimization problem, the Lagrangian of the objective function is defined as:

$$L = J + a(\mathbf{u}, \mathbf{w}, \boldsymbol{\Phi}^{\mathbf{geo}}) - l(\mathbf{w}, \boldsymbol{\Phi}^{\mathbf{geo}}) \tag{9}$$

where $\mathbf{w}$ is the Lagrangian multiplier of the state equation, also known as adjoint variable. Compliance minimization can be categorized as self-adjoint problem which satisfies that $\mathbf{w_k} = -2\mathbf{u_k}$.

Then, the derivative of the Langrangian is:

$$L' = 2\sum_{k=1}^{N} \int_{D_k} \mathbf{D_k e}\left(\mathbf{u^{in}}(\boldsymbol{\theta}^{\mathbf{k}})\right)' \mathbf{e}(\mathbf{u_k})\, H(\phi^{geo,k}) d\Omega \tag{10}$$

The derivative term of the inherent strain, $\mathbf{e}\left(\mathbf{u^{in}}(\boldsymbol{\theta}^{\mathbf{k}})\right)'$ could be rewritten as:

$$\mathbf{e}\left(\mathbf{u^{in}}(\boldsymbol{\theta}^{\mathbf{k}})\right)' = \frac{\partial \boldsymbol{\varepsilon}^{\mathbf{in,k}}}{\partial \boldsymbol{\theta}^{\mathbf{k}}} \frac{\partial \boldsymbol{\theta}^{\mathbf{k}}}{\partial \phi^{scan,k}} \frac{\partial \phi^{scan,k}}{\partial t} \tag{11}$$

The expression for $\theta^k$ is defined as:

$$\boldsymbol{\theta}^{\mathbf{k}} = \frac{\pi}{2} + \arctan\left(\frac{\partial \phi^{scan,k}/\partial \mathrm{y}}{\partial \phi^{scan,k}/\partial \mathrm{y}}\right) \tag{12}$$

Specifically, for node $(i, j, k)$, the scanning orientation, $\theta_{i,j}^{k}$ is derived using the central difference scheme:

$$\theta_{i,j}^{k} = \frac{\pi}{2} + \arctan\left(\frac{\phi_{i,j+1}^{scan,k} - \phi_{i,j-1}^{scan,k}}{\phi_{i+1,j}^{scan,k} - \phi_{i-1,j}^{scan,k}}\right) \tag{13}$$

Therefore, derivative of the inherent strains is expressed as:

$$\mathbf{e}\left(\mathbf{u}_{\mathbf{i,j}}^{\mathbf{in}}(\boldsymbol{\theta}^{\mathbf{k}})\right)' = \frac{\partial \boldsymbol{\varepsilon}_{\mathbf{i,j}}^{\mathbf{in,k}}}{\partial \theta_{i,j}^{k}} \frac{\partial \theta_{i,j}^{k}}{\partial \phi_{i-1,j}^{scan,k}} \frac{\partial \phi_{i-1,j}^{scan,k}}{\partial t} + \frac{\partial \boldsymbol{\varepsilon}_{\mathbf{i,j}}^{\mathbf{in,k}}}{\partial \theta_{i,j}^{k}} \frac{\partial \theta_{i,j}^{k}}{\partial \phi_{i+1,j}^{scan,k}} \frac{\partial \phi_{i+1,j}^{scan,k}}{\partial t} + \frac{\partial \boldsymbol{\varepsilon}_{\mathbf{i,j}}^{\mathbf{in,k}}}{\partial \theta_{i,j}^{k}} \frac{\partial \theta_{i,j}^{k}}{\partial \phi_{i,j-1}^{scan,k}} \frac{\partial \phi_{i,j-1}^{scan,k}}{\partial t} + \frac{\partial \boldsymbol{\varepsilon}_{\mathbf{i,j}}^{\mathbf{in,k}}}{\partial \theta_{i,j}^{k}} \frac{\partial \theta_{i,j}^{k}}{\partial \phi_{i,j+1}^{scan,k}} \frac{\partial \phi_{i,j+1}^{scan,k}}{\partial t} \tag{14}$$

Collecting all the terms containing $\frac{\partial \phi_{i,j}^{scan,k}}{\partial t}$, the scanning path level set function updated velocity at node $(i,j,k)$ can be derived:

$$\begin{aligned} V_{N\,i,j}^{scan,k} = 2\Bigg\{ & \mathbf{D_k e}\left(\mathbf{u}_{\mathbf{i-1,j}}^{\mathbf{k}}\right) \frac{\partial \boldsymbol{\varepsilon}_{\mathbf{i-1,j}}^{\mathbf{in,k}}}{\partial \theta_{i-1,j}^{k}} \frac{\partial \theta_{i-1,j}^{k}}{\partial \phi_{i,j}^{scan,k}} H\left(\phi_{i-1,j}^{scan,k}\right) \\ & + \mathbf{D_k e}\left(\mathbf{u}_{\mathbf{i+1,j}}^{\mathbf{k}}\right) \frac{\partial \boldsymbol{\varepsilon}_{\mathbf{i+1,j}}^{\mathbf{in,k}}}{\partial \theta_{i+1,j}^{k}} \frac{\partial \theta_{i+1,j}^{k}}{\partial \phi_{i,j}^{scan,k}} H\left(\phi_{i+1,j}^{scan,k}\right) \\ & + \mathbf{D_k e}\left(\mathbf{u}_{\mathbf{i,j-1}}^{\mathbf{k}}\right) \frac{\partial \boldsymbol{\varepsilon}_{\mathbf{i,j-1}}^{\mathbf{in,k}}}{\partial \theta_{i,j-1}^{k}} \frac{\partial \theta_{i,j-1}^{k}}{\partial \phi_{i,j}^{scan,k}} H\left(\phi_{i,j-1}^{scan,k}\right) \\ & + \mathbf{D_k e}\left(\mathbf{u}_{\mathbf{i,j+1}}^{\mathbf{k}}\right) \frac{\partial \boldsymbol{\varepsilon}_{\mathbf{i,j+1}}^{\mathbf{in,k}}}{\partial \theta_{i,j+1}^{k}} \frac{\partial \theta_{i,j+1}^{k}}{\partial \phi_{i,j}^{scan,k}} H\left(\phi_{i,j+1}^{scan,k}\right) \Bigg\} \end{aligned} \tag{15}$$

### 3.3 Stress minimization

The potential of laser deposition path optimization in minimizing residual stress is explored as well. Stress concentration can be mitigated and consequently prevent cracking and delamination during AM processing. To achieve this, the maximum von Mises stress within the AM part should be decreased by optimizing the scanning path. However, the simple maximum function is not smooth and differentiable and cannot be applied directly to gradient-based optimization. The p-norm function [51, 52], an alternative formulation for maximum stress approximation in stress-based topology optimization, is adopted in this framework as:

$$\sigma_{PN} = \left(\sum_{e=1}^{N} \sigma_e^P\right)^{\frac{1}{P}} \tag{16}$$

where $\sigma_{PN}$ is the p-norm stress, $\sigma_e$ is the element stress, $N$ is the total element number, and $P$ is the stress norm parameter. When $P \to \infty$, $\sigma_{PN} \to \max(\sigma_e)$ without smoothness; when $P \to 1$, $\sigma_{PN}$ is the average stress of the design domain. It is noted that for stress minimization problem of interest in this work, the stress norm parameter $P$ is not as critical as in stress constrained problems, since it is sufficient for the p-norm stress to capture the trend of the global maximum stress rather than having an accurate approximation [51]. In this work, the value of the stress norm parameter $P$ is taken as 8 in the stress minimization problem.

Stress at the element centroid is selected as the average element stress $\sigma_e$ in computing the element von Mises stress. The residual stress minimization problem is formulated as:

$$min.\,\sigma_{PN} = \left[\sum_{k=1}^{n}\int_{D_k}\sigma_{von}^{P}\,H(\phi^{geo,k})d\Omega\right]^{\frac{1}{P}} \qquad (17)$$
$$s.t.\,a(\mathbf{u},\mathbf{v},\boldsymbol{\Phi}^{\mathbf{geo}}) = l(\mathbf{v},\boldsymbol{\Phi}^{\mathbf{geo}}),\quad \forall\mathbf{v}\in\mathbf{U_{ad}}$$

The derivative of the above Lagrangian is shown below:

$$L' = -\sum_{k=1}^{n}\int_{D_k}\mathbf{D_k}\mathbf{e}\,(\mathbf{u^{in}}(\theta^k)')\,\mathbf{e}(\mathbf{w_k})H(\phi^{geo,k})d\Omega \qquad (18)$$

where the adjoint variable $\mathbf{w_k}$ can be obtained by solving the following adjoint equation:

$$\sum_{k=1}^{n}\int_{D_k}\mathbf{D_k}\mathbf{e}(\mathbf{u_k'})\mathbf{e}(\mathbf{w_k})\,H(\phi^{geo,k})d\Omega + \left[\sum_{k=1}^{n}\int_{D_k}\sigma_{von}^{P}\,H(\phi^{geo,k})d\Omega\right]^{\frac{1}{P}-1} \cdot\left[\sum_{k=1}^{n}\int_{D_k}\sigma_{von}^{P-1}\cdot\sigma_{von}'\,H(\phi^{geo,k})d\Omega\right] = 0 \qquad (19)$$

Expanding all the inherent strain derivative terms $\mathbf{e}(\mathbf{u^{in}}(\theta^k)')$ in the Lagrangian**,** and collecting all the terms containing $\frac{\partial\phi_{i,j}^{scan,k}}{\partial t}$, the sensitivity at node$(i,j,k)$, namely the level set function updated velocity along the normal direction can be derived:

$$V_{N}{}_{i,j}^{scan,k} = \left\{\mathbf{e}\left(\mathbf{w_{k,i-1,j}}\right)'\,\mathbf{D_k}\frac{\partial\boldsymbol{\varepsilon}_{\mathbf{i-1,j}}^{\mathbf{in,k}}}{\partial\theta_{i-1,j}^{k}}\cdot\frac{\partial\theta_{i-1,j}^{k}}{\partial\phi_{i,j}^{scan,k}}\cdot\frac{\partial\phi_{i,j}^{scan,k}}{\partial t} + \mathbf{e}\left(\mathbf{w_{k,i+1,j}}\right)'\,\mathbf{D_k}\frac{\partial\boldsymbol{\varepsilon}_{\mathbf{i+1,j}}^{\mathbf{in,k}}}{\partial\theta_{i+1,j}^{k}}\cdot\frac{\partial\theta_{i+1,j}^{k}}{\partial\phi_{i,j}^{scan,k}} \cdot\frac{\partial\phi_{i,j}^{scan,k}}{\partial t} + \mathbf{e}\left(\mathbf{w_{k,i,j-1}}\right)'\,\mathbf{D_k}\frac{\partial\boldsymbol{\varepsilon}_{\mathbf{i,j-1}}^{\mathbf{in,k}}}{\partial\theta_{i,j-1}^{k}}\cdot\frac{\partial\theta_{i,j-1}^{k}}{\partial\phi_{i,j}^{scan,k}}\cdot\frac{\partial\phi_{i,j}^{scan,k}}{\partial t} + \mathbf{e}\left(\mathbf{w_{k,i,j+1}}\right)'\,\mathbf{D_k}\frac{\partial\boldsymbol{\varepsilon}_{\mathbf{i,j+1}}^{\mathbf{in,k}}}{\partial\theta_{i,j+1}^{k}}\cdot\frac{\partial\theta_{i,j+1}^{k}}{\partial\phi_{i,j}^{scan,k}}\cdot\frac{\partial\phi_{i,j}^{scan,k}}{\partial t}\right\} \qquad (20)$$

## 4. Adaptive level set adjustment (ALSA)

Signed distance function is a fundamental feature of the level set method. It ensures the easiness and effectiveness of the numerical contour evolution. Importantly for this research, continuous scanning paths with consistent gaps (i.e. hatching space) can be trivially derived by extracting the iso-level set contours. Therefore, reinitialization, which adjusts the level set function based on the interface ($\phi = 0$) as mentioned in Section 3.1, is implemented in each iteration step to enforce the updated level set function to be a signed-distance field. However, one issue occurs due to reintialization and should be carefully addressed to ensure the proper

convergence. Specifically, the velocity field, as derived in Eq. (15) and (20), is defined inside the entire material domain, and the whole level set field can be accordingly updated by solving the Hamilton-Jacobi equation. At this point, the Lagrangian is strictly decreasing with appropriate step size. However, reinitialization has to be performed following the design update to ensure a signed distance field, so that level set values in areas away from the interface will be altered. The impact of these changes is hard to evaluate and it is possible that the Lagrangian will increase. Conventionally in topology optimization, it is common to neglect the impact of these changes, and many cases of successful convergence have been witnessed, especially for compliance minimization problems [19, 20]. This is because, in topology optimization, the zero-value level set contour is the boundary between solid and void and its movement also changes the material layout. However, for the scanning path optimization, the zero level set contour does not represent the structure boundary; instead, it only represents one of the scanning lines and only the relevant scanning orientation affects the stress and deformation. The shrinkage of zero level set contour and decreasing perimeter is undesirable since the zero level set contour is the only effective updating scanning line while all the other scanning lines follow the shape of the zero level set contour because of the reinitialization. Therefore, maintaining as longer zero level set contour as possible motivates the development of the adaptive level set adjustment (ALSA) strategy. Similarly, over-expansion of the zero level set contour is also undesirable since all zero level set contour moves towards outside of the design domain, which may finally leave no zero contour inside the design domain for effective design update. Specifically in ALSA, what we are adjusting is only the level set values of the contours while not the shape of the contours. Therefore, the finite difference method-based local scanning direction calculation would not be affected, so that the inherent strain-based finite element analysis result would be identical before and after adaptive change of the level set field.

In this work, a numerical strategy called the "adaptive level set adjustment" (ALSA) is proposed to reduce the potential negative impact, instead of just neglecting it. Using this technique, good convergence for complex continuous path optimization problems have been realized for both compliance- and stress-minimization problems. The basic idea of the ALSA strategy is to keep as much zero level set contour as possible inside the design domain during the entire optimization process, because the zero level set contour would not be affected by reinitialization. In fact, in some of the runs, we have observed that the zero level set contour keeps shrinking, which finally occupies a very small portion of the design domain and leads the optimization problem fails to converge in this situation. To remedy this issue, the ALSA adjusts the zero level set contour iteratively with Eq. (21):

$$\phi^{scan,k} = \begin{cases} \phi^{scan,k} - \alpha \cdot \phi_{max}^{scan,k}, & S_+ > S_- \\ \phi^{scan,k} - \alpha \cdot \phi_{min}^{scan,k}, & S_+ < S_- \end{cases} \tag{21}$$

where $\phi_{max}^{scan,k}$ is the maximum level set nodal value in layer $k$, $\phi_{min}^{scan,k}$ is the minimum nodal value, $S_+$ is the area of positive level set field, $S_-$ is the area of negative level set field, and $\alpha$ $(0 < \alpha < 1)$ is the coefficient for level set function adjustment.

The physical meaning of ALSA is that the level set function is iteratively adjusted to equalize the positive-signed area and the negative-signed area, which in most cases could function to give a longer zero level set contour while not perturbing the scanning path field. While with ALSA, the zero level set interface will be dynamically adjusted to prevent this type of over-shrinking situation. Figure 1 illustrates an example to show the effectiveness of applying the ALSA strategy. As shown in Fig. 1(a), the initial scanning path is designed to have as longer zero level set contour as possible, so that to ensure effective and efficient design update. As discussed before, only the boundary update is effective, thus only the sensitivities near the zero level set contour are calculated and shown in this case. After 20 iterations, Fig. 1(b) still holds a large area of zero level set interface by employing the ALSA strategy. In contrast, as shown in Fig. 1(c), the level set field moves outward and the zero-value interface keeps shrinking to very small closed contours without ALSA. Then, the design update effect of the later is quite questionable.

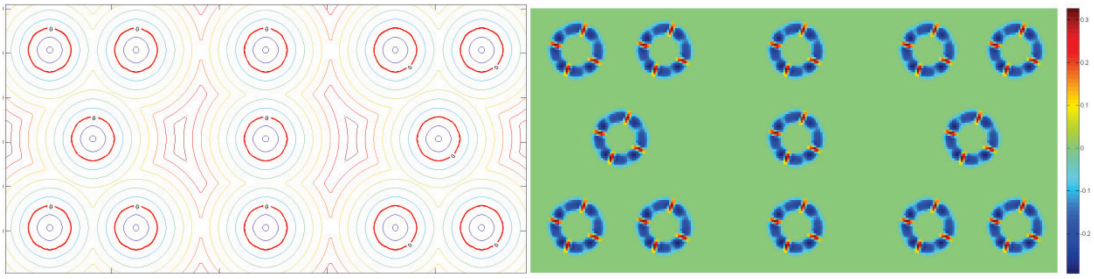

(a)

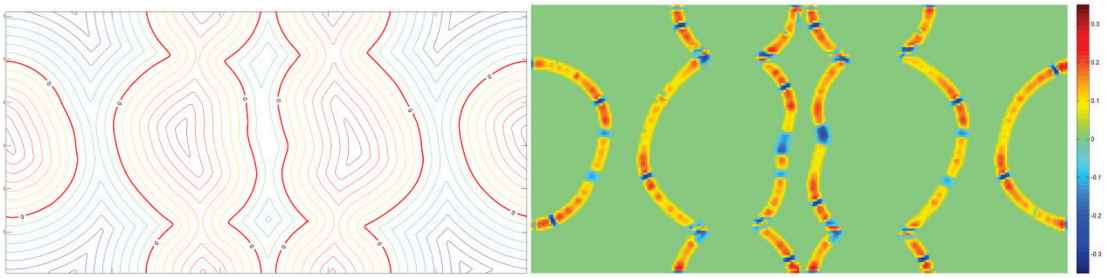

(b)

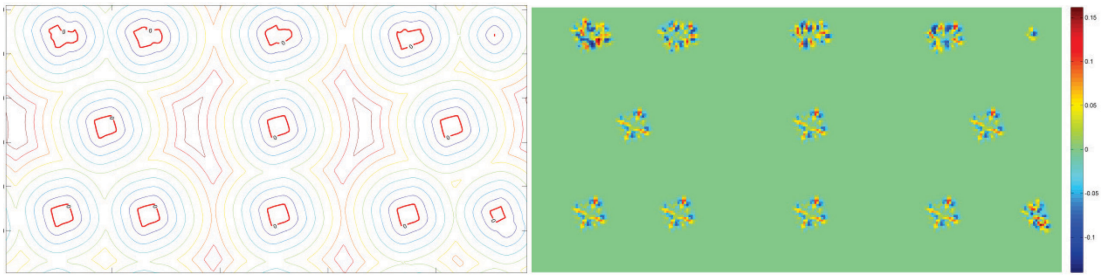

(c)

**Figure 1** Sensitivity distribution (a) Initial scanning path setup; (b) with ALSA; (c) without ALSA

With the sensitivity analysis and ALSA strategy at hand, a step by step description for scanning path optimization is outlined:

1. Develop the finite element model and initialize the scanning path of each layer.
2. Calculate the scanning orientation of each element from Eq. (13).
3. Calculate the nodal force vector from Eq. (1) and assemble the global force vector F.
4. Solve the finite element problem.
5. Derive the normal velocity $V_{N_{i,j}}^{scan,k}$ from Eq. (15) or (20).
6. Update the level set filed with normal velocity by solving the Hamilton-Jacobi equation.
7. Reinitialize and modify the level set field with ALSA by Eq. (21).
8. Check for convergence criteria; If not satisfied, return to step 2.

## 5. Numerical examples

In this section, the proposed algorithm will be demonstrated using a few numerical examples to prove its effectiveness. In all of the following numerical examples, we assume the material has a Young's modulus of 2,100 and Poisson's ratio of 0.3. All the design domains are discretized by 1×1×1 eight-node hexahedron mesh with 24 DoFs.

### 5.1 Compliance minimization

Case 1: The first case is compliance minimization of an L-bracket structure. The dimension and finite element mesh of the L-bracket is shown in Fig. 2(a). There are a total of four bundled printing layers, and the bottom nodes are fixed on the build plate. The scanning orientation-dependent inherent strain vector of [-0.0145, -0.0065, 0.012] is applied as the loading. The initial scanning path setup before optimization is shown in Fig. 2(b), where the thermal loading induced compliance is 1,147.

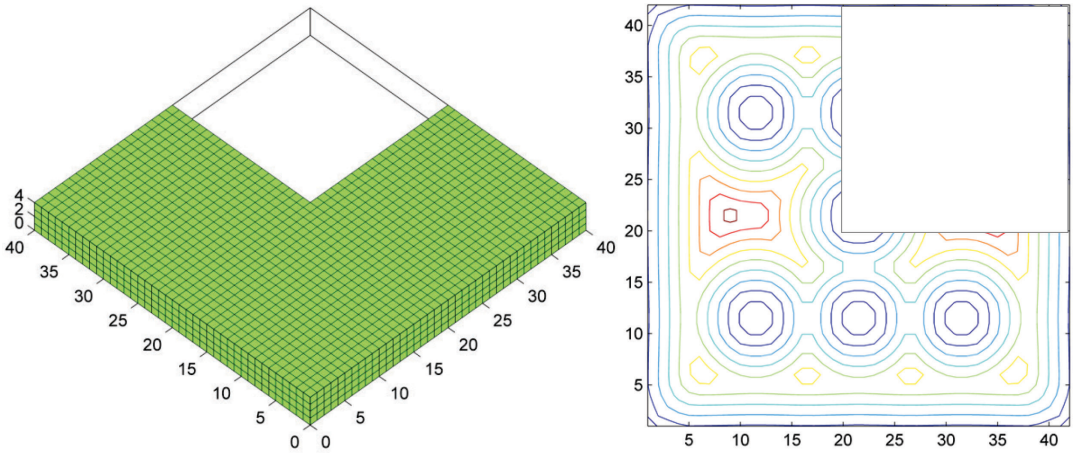

(a) Finite element model of the L-bracket (b) Initial scanning path of each layer

**Figure 2** Initial setup of the L-bracket optimization (Compliance 1,147)

The optimized scanning path of each layer is presented in Fig .3. Compared with the previous optimized scanning path by either experiment or simulation, this scanning path is irregular and counter-intuitive. The convergence history is shown in Fig .4. The structural compliance is reduced by 15.4% (from 1,147 to 970) after optimization.

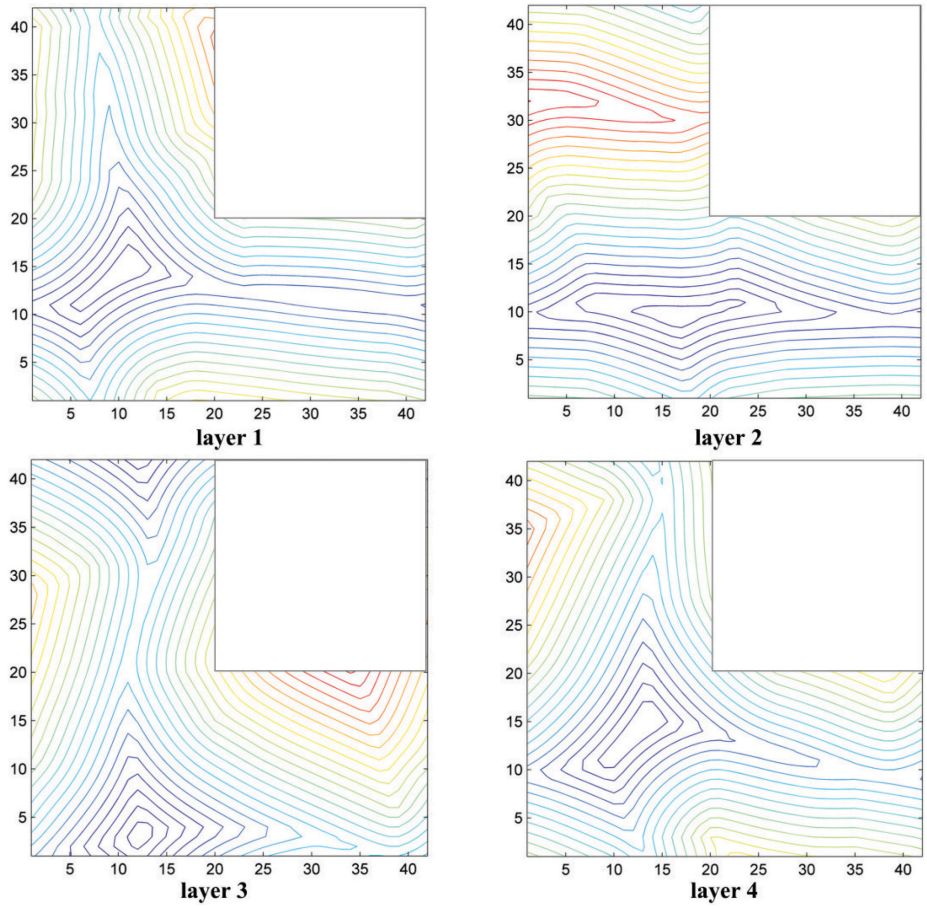


**Figure 3** Layer-wise deposition optimization results for L-bracket

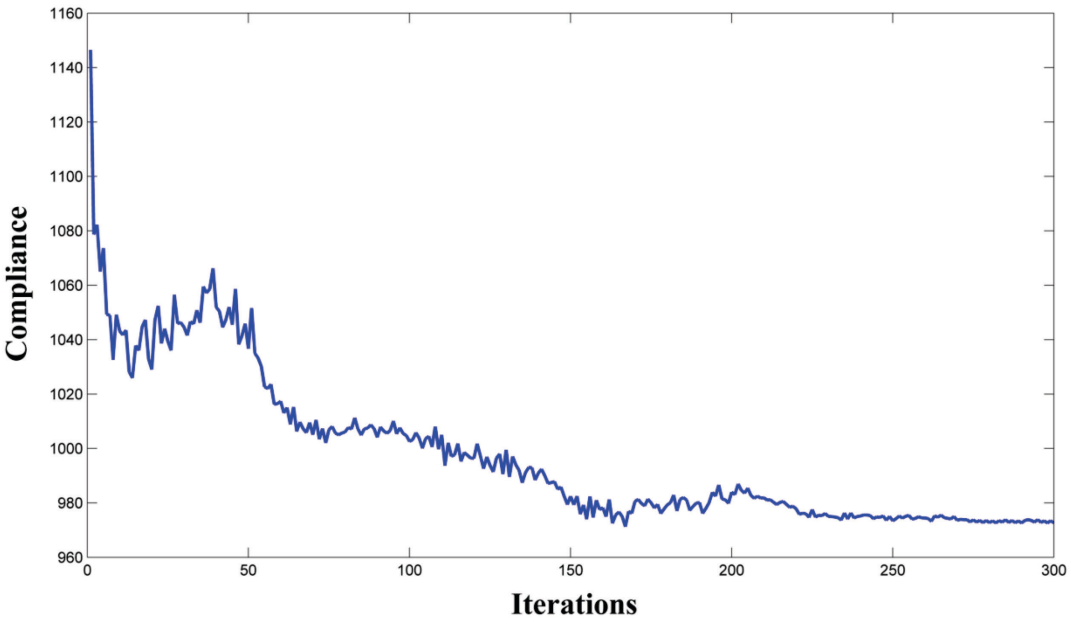


**Figure 4** Convergence history of the L-bracket compliance minimization case

The layer-wise compliance of the four-layer L-bracket case before and after scanning path optimization is presented in Fig. 5. It can be found that a global compliance minimization is achieved by optimizing laser scanning paths. The structural compliance is reduced by 16.0% for layer 1, 16.0% for layer 2, 16.9% for layer 3 and 13.0% for layer 4, respectively.

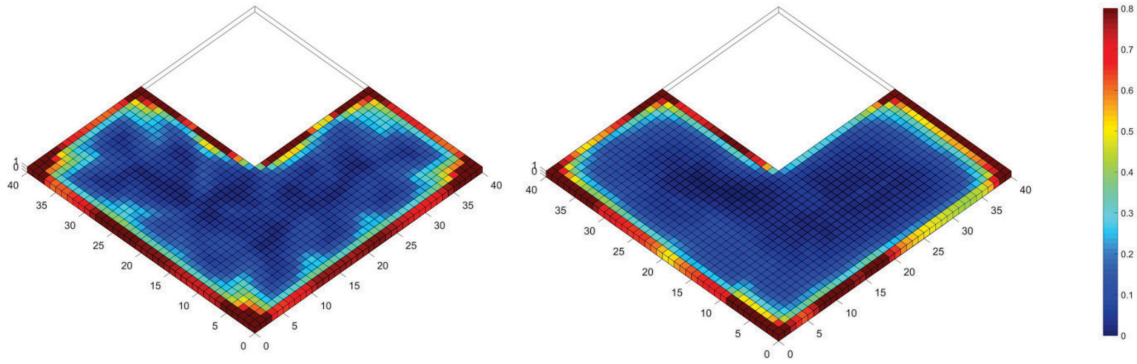

before optimization
layer-wise compliance:309.53

after optimization
layer-wise compliance:260.06

(a) Layer 1

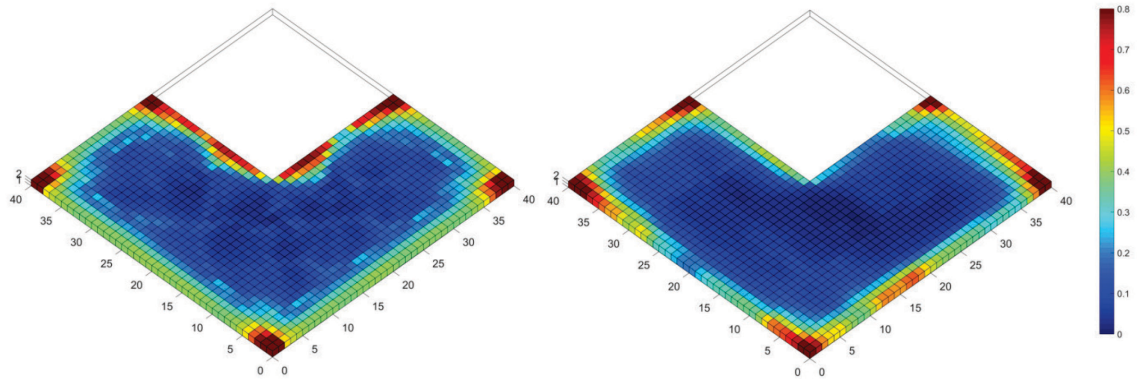

before optimization
layer-wise compliance:267.91

after optimization
layer-wise compliance:225.13

(b) Layer 2

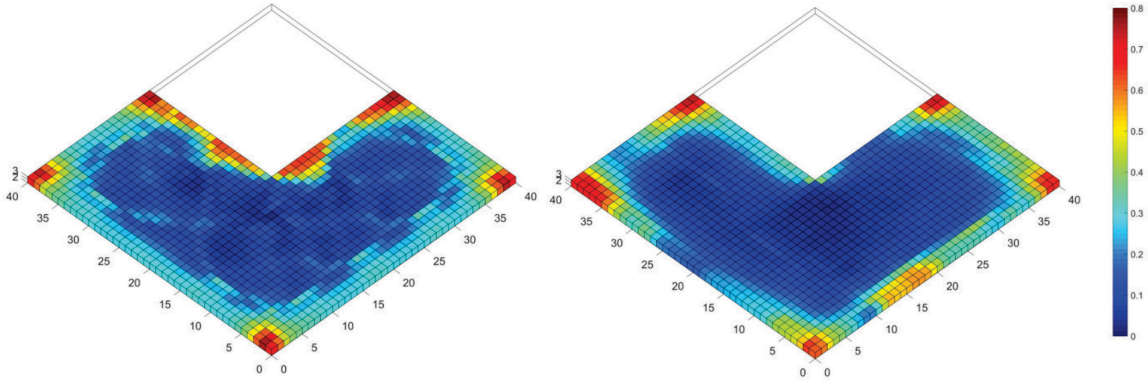

before optimization
layer-wise compliance:280.03

after optimization
layer-wise compliance:232.82

(c) Layer 3

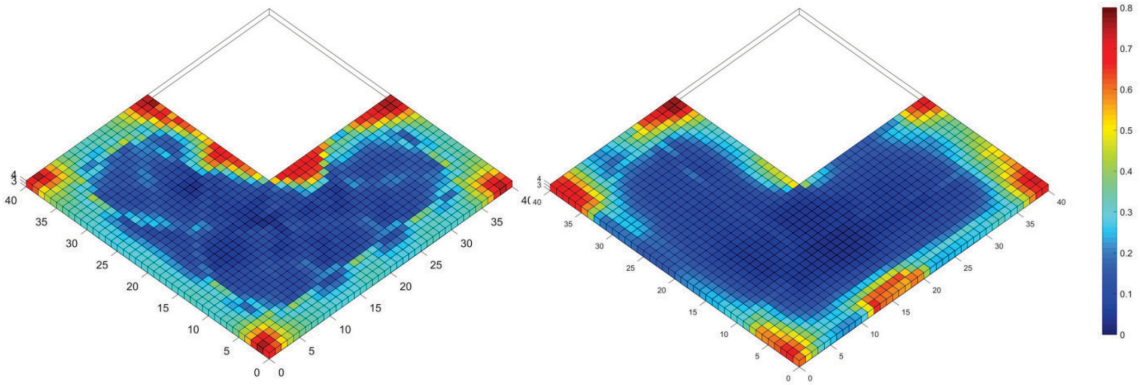

before optimization
layer-wise compliance:289.53

after optimization
layer-wise compliance:252.01

(d) Layer 4

**Figure 5** Layer-wise compliance comparison before and after optimization

Besides the layer-wise compliance analysis, the comparison of layer-wise von Mises stress profile before and after compliance minimization is given in Fig. 6 for better interpretation of the proposed scanning path optimization. It can be found that after compliance minimization, the global maximum stress located in the bottom layer is reduced from 73.4 to 68.2. The stress concentration at the corner of the L-bracket can be mitigated as well by compliance minimization since the displacement has also been reduced.

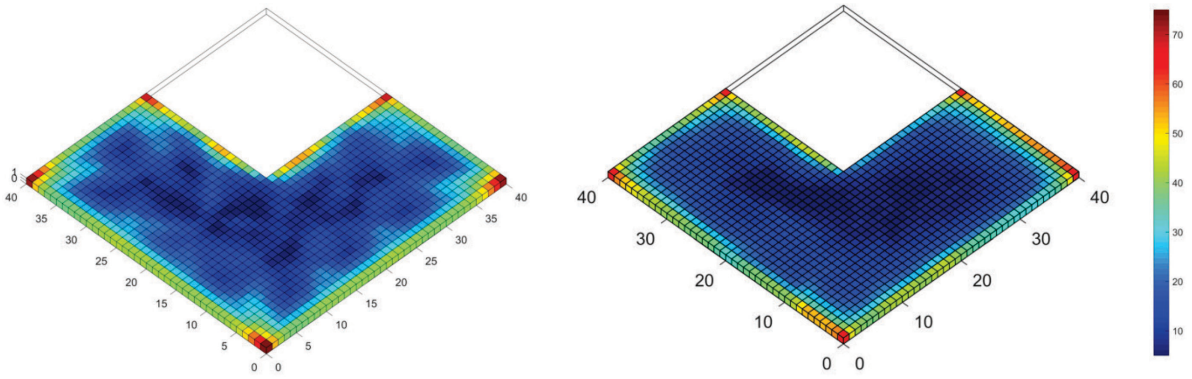

before optimization
layer-wise maximum von Mises stress: 73.54

after optimization
layer-wise maximum von Mises stress: 68.24

(a) Layer 1

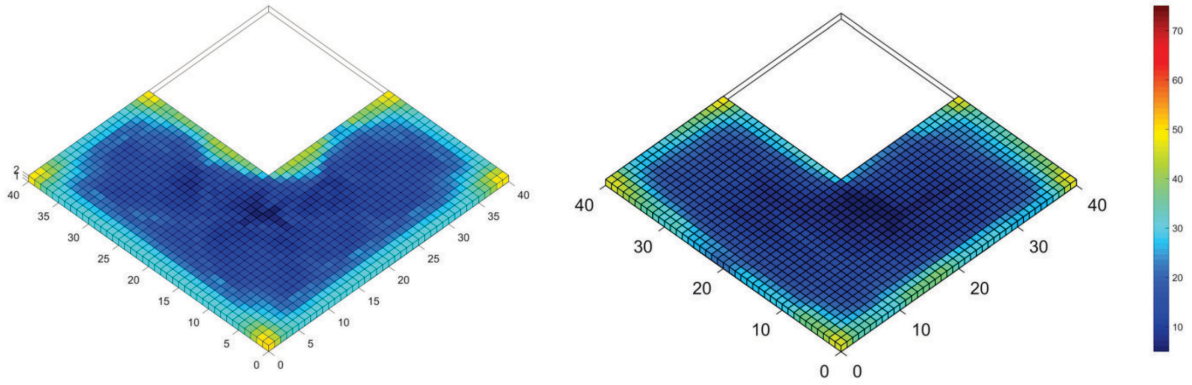

before optimization
layer-wise maximum von Mises stress: 50.02

after optimization
layer-wise maximum von Mises stress: 48.19

(b) Layer 2

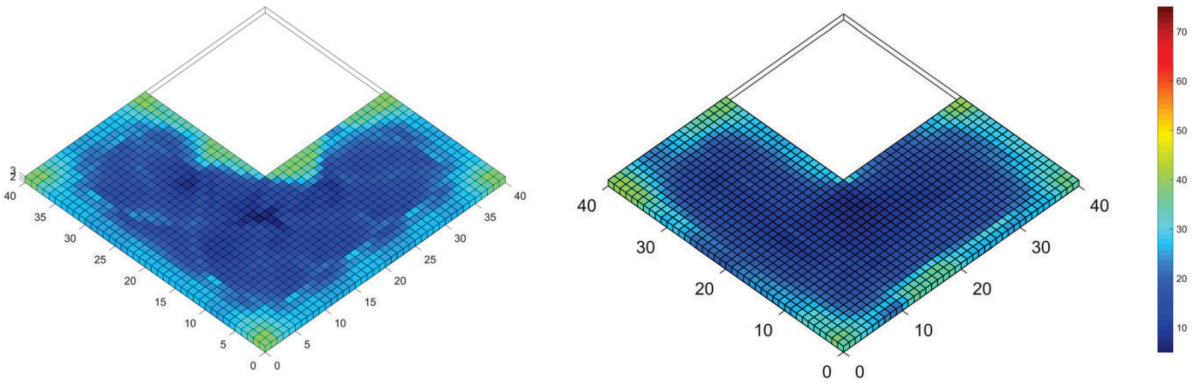

before optimization
layer-wise maximum von Mises stress: 39.76

after optimization
layer-wise maximum von Mises stress: 40.62

(c) Layer 3

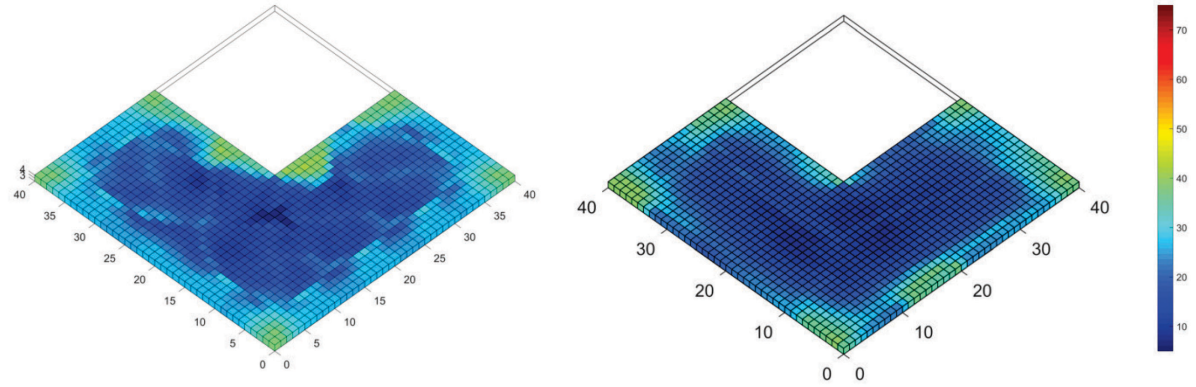

before optimization
layer-wise maximum von Mises stress: 41.15

after optimization
layer-wise maximum von Mises stress: 39.50

(d) Layer 4

**Figure 6** Layer-wise von Mises stress comparison before and after optimization

Case 2: The second case is on compliance minimization of a 60×30×4 block with two semi-circular holes and two internal holes, the radius of which is all 5. The dimension and finite element mesh of the block is shown in Fig. 7(a) and the bottom nodes are fixed. The inherent strain vector applied is still [-0.0145, -0.0065, 0.012]. Two different initial guesses of the scanning paths are employed as demonstrated in Fig. 7(b)-(c) to for the initial set up dependency study. Thermal loading induced compliance is 1,492 with initial set up 1 and 1,702 with initial set up 2, respectively.

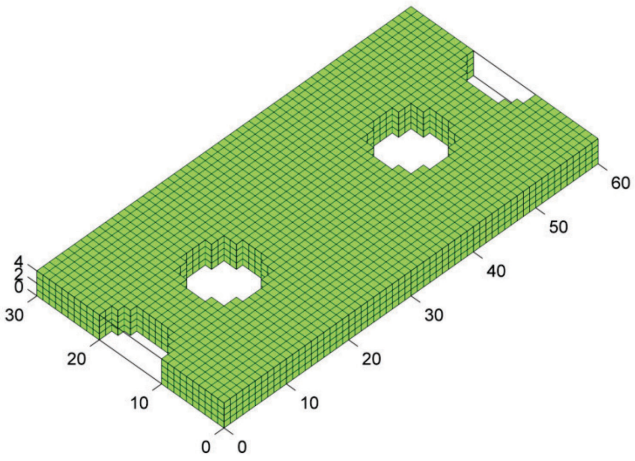


(a) Finite element model of block

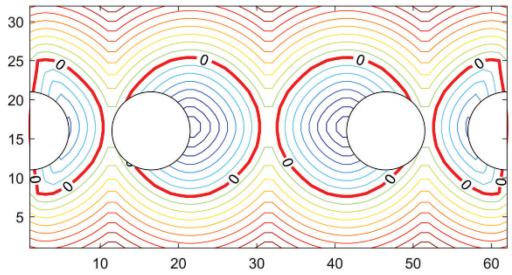


(b) Initial scanning path set up 1

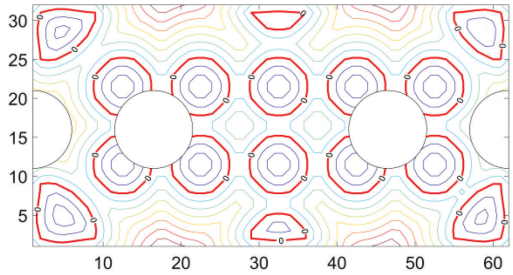


(c) Initial scanning path set up 2

**Figure 7** Initial setup of the block with internal holes optimization

The layer-wise optimized laser scanning paths and convergence history are presented in Fig. 8 and Fig. 9 for initial scanning path 1, and in Fig. 10 and Fig. 11 for initial scanning path 2, respectively. Although different initial scanning paths are employed, the optimization processes ends up with very similar results that the optimized scanning paths in each layer have a dominant trend in horizontal direction as shown in Fig. 8 and Fig. 10. The optimized structural compliance of initial guess 1 is 1,250, and the optimized structural compliance of initial guess 2 is 1,257. However, it is worth noting that there are still different local features between the two optimized scanning paths due to initial paths, which indicates that there are multiple optimal solutions when the structural compliance is around 1,250. Therefore, the proposed algorithm has the initial guess dependency issue, but is able to converge to local optimum solutions with similar laser scanning path distribution and close overall distortion, which is true at least for the current example. Through external thermal loading adjustment, structure compliance is minimized, and this 4-layer block under the optimized scanning path is less prone to bending or deformation under the laser scanning induced thermal loading.

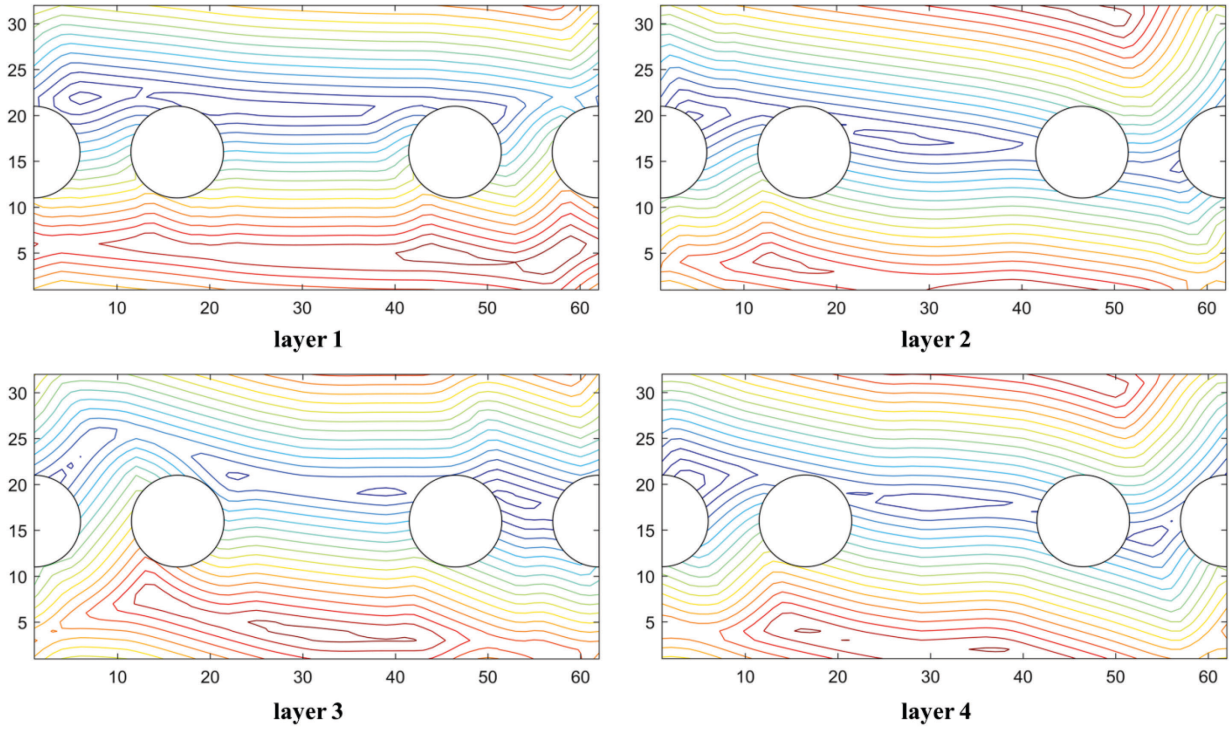


**Figure 8** Layer-wise deposition optimization results for the 4-layer block with initial set up 1

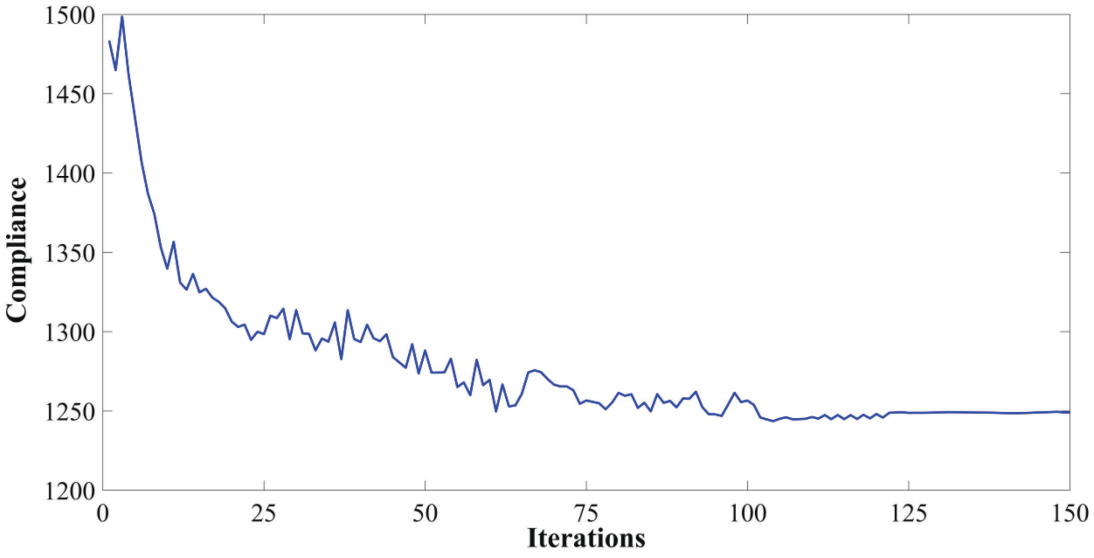


**Figure 9** Convergence history of the block compliance minimization case with initial set up 1

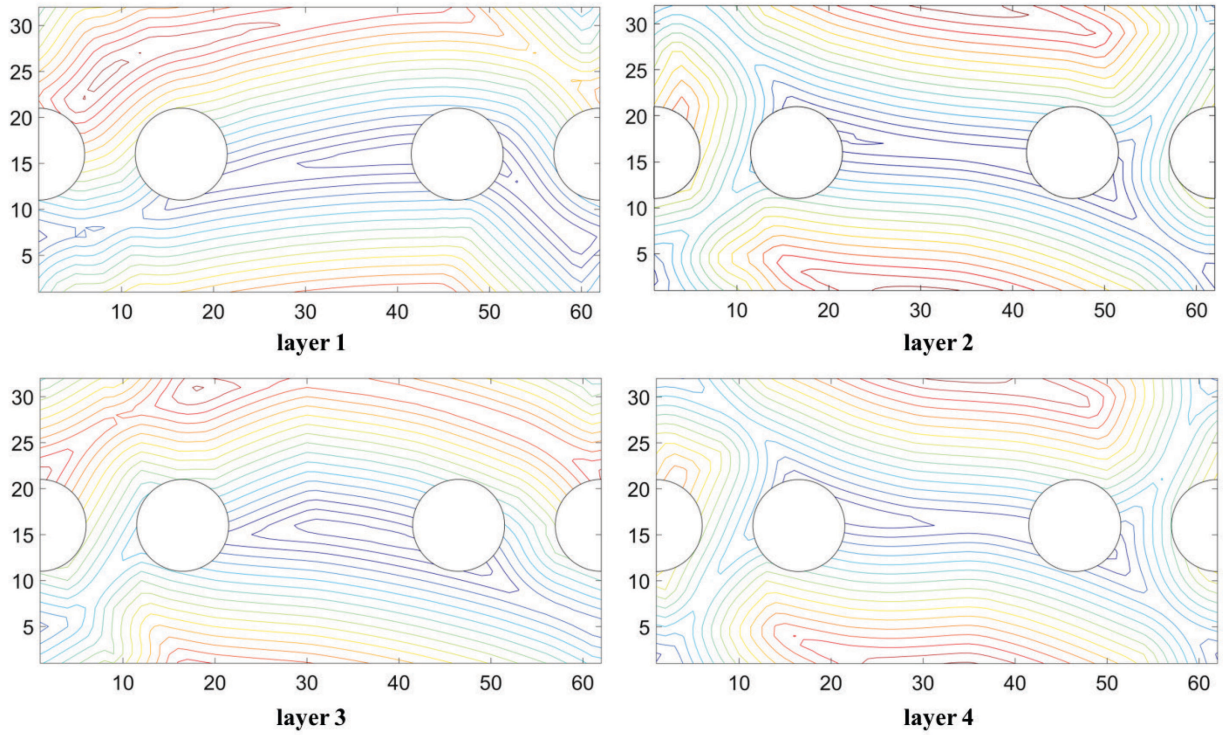


**Figure 10** Layer-wise deposition optimization results for the 4-layer block with initial set up 2

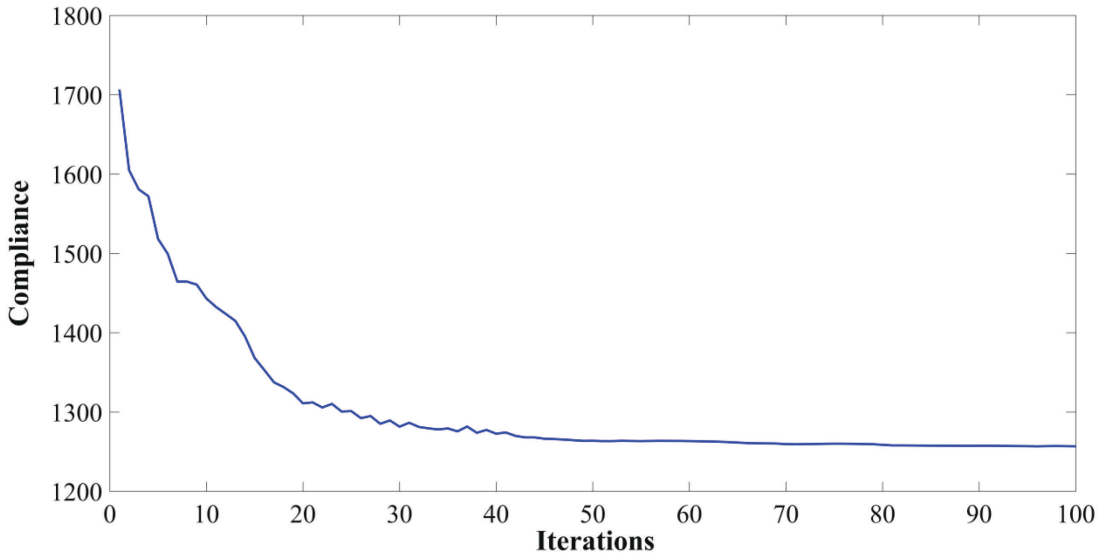


**Figure 11** Convergence history of the block compliance minimization case with initial set up 2

Case 3: The third compliance minimization case is on a bearing bracket consisting of 35 layers as shown in Fig. 12(a). The same inherent strain vector and the same type of initial scanning path is utilized as shown in Fig 12(b).

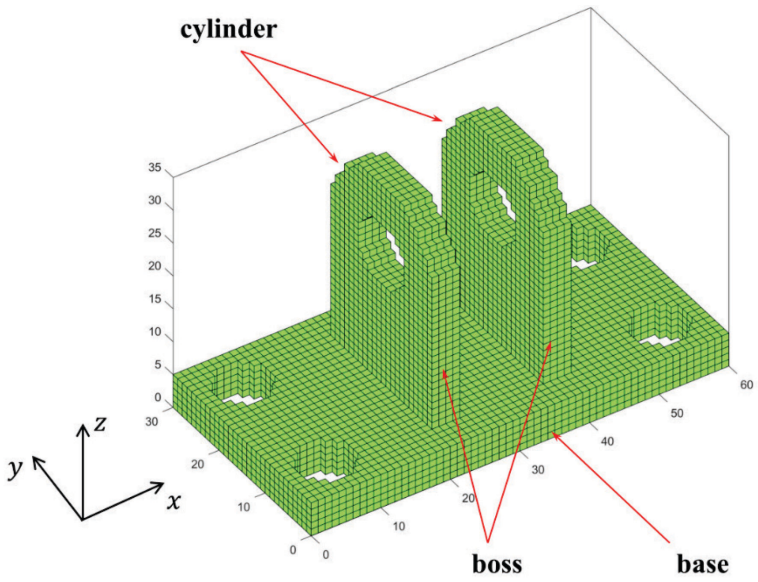


(a) Finite element model of the bearing bracket

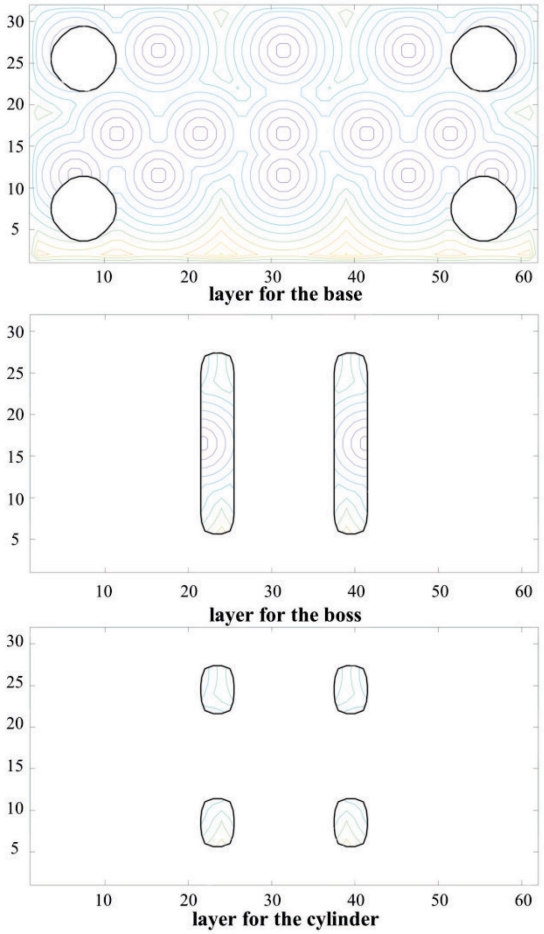


(b) Initial scanning path of each component

**Figure 12** Initial setup of the bearing bracket optimization (Compliance 5,267)

The optimization converges with 100 iterations. The compliance has reduced from 5,267 to 4,633. The optimized scanning paths patterns for layer 1, 5, 11, 22, 30 and 34 are presented in Fig. 13. Repeated scanning pattern is not found among the layers. The comparison with initial scanning path in Fig. 12(b) indicates that the scanning pattern of each layer is optimized to achieve an optimized optimal solution after exploring the design space. The convergence history is summarized in Fig. 14.

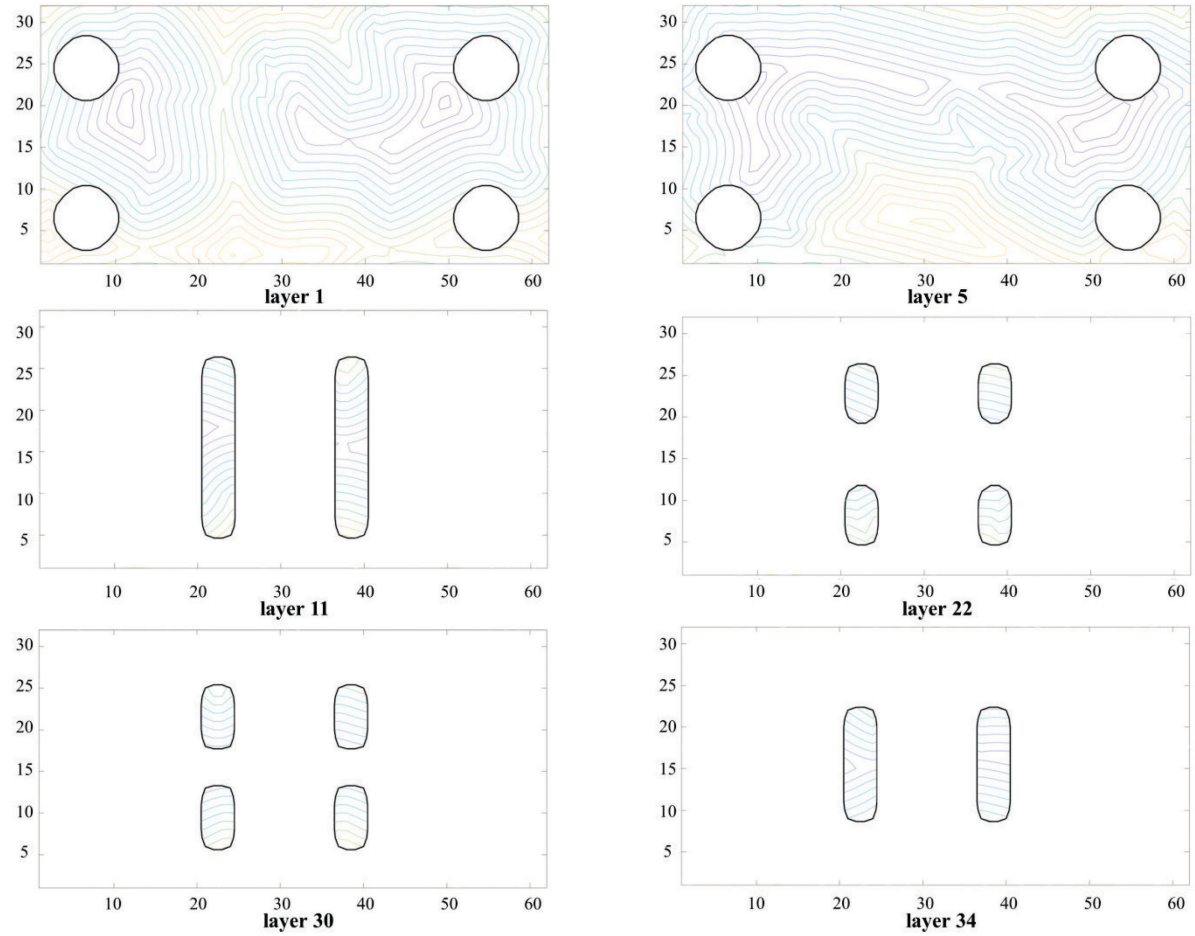


**Figure 13** Layer-wise scanning path after optimization for the bearing bracket

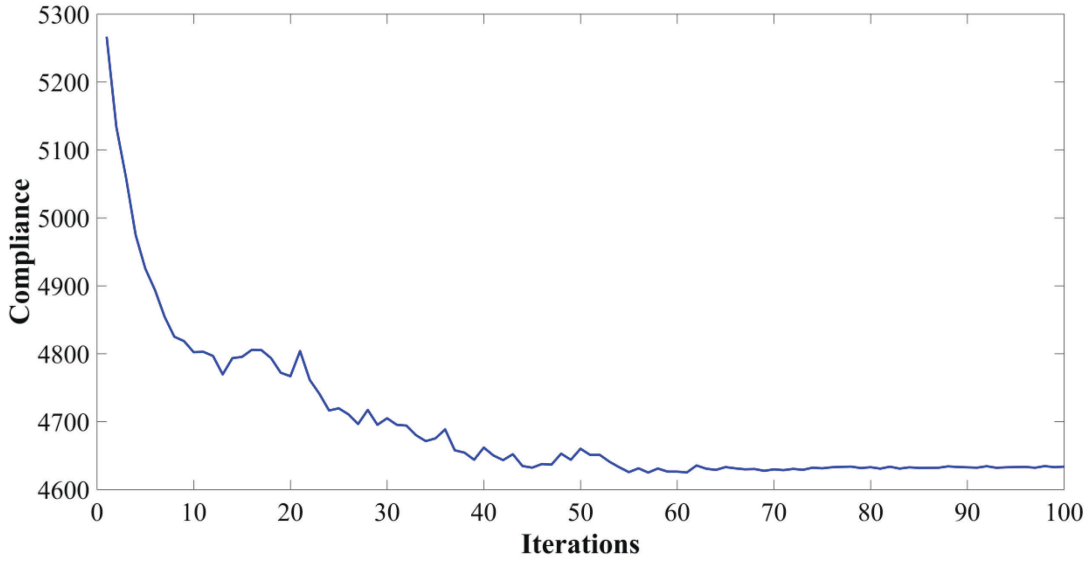


**Figure 14** Convergence history of the bearing bracket case

### 5.2 Stress minimization

Case 4: Stress optimization is performed on the same L-bracket as shown in Fig. 2(a), and the same initial scanning path of Fig. 2(b) is adopted. The optimized laser deposition path is presented in Fig. 15, and the convergence history is plotted in Fig. 16. It can be found that the p-norm stress is reduced from 98.8 to 92.3 after 100 iterations. As for the maximum von Mises stress, it decreases from 73.6 to 65.4. Oscillations in the stress convergence history have been observed, which is common for stress-based optimization. With the reduced stress level, failures such as delamination and cracking are less prone to occur.

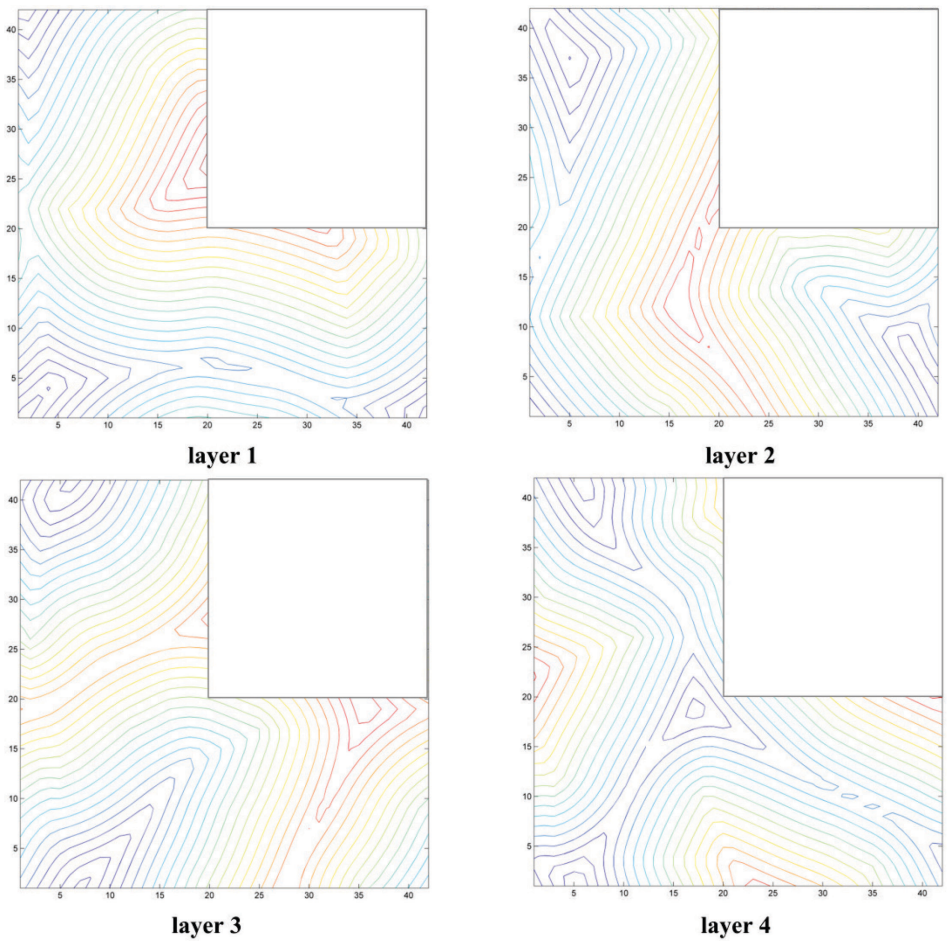


**Figure 15** Layer-wise scanning path of the L-bracket

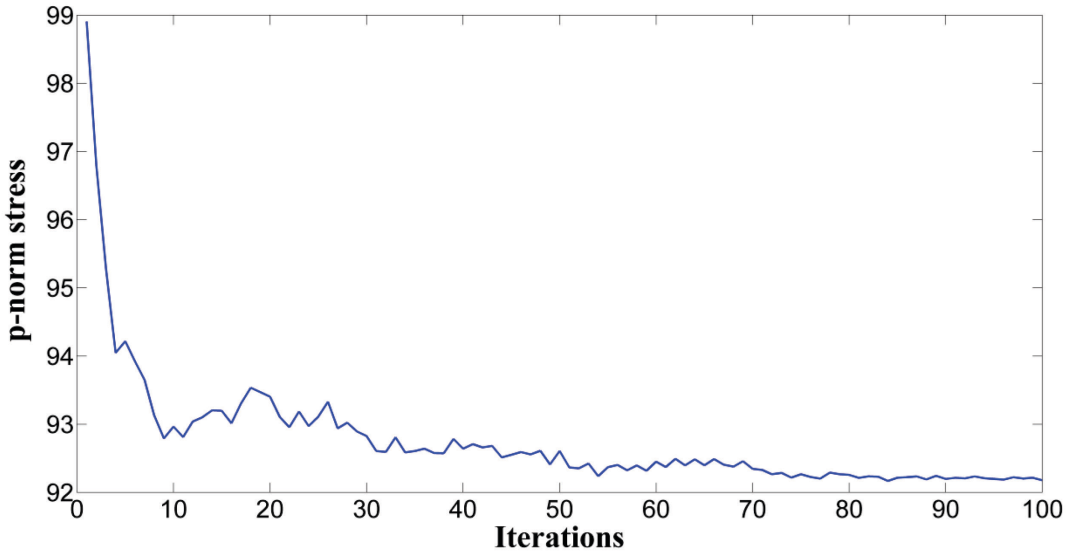


(a) p-norm stress

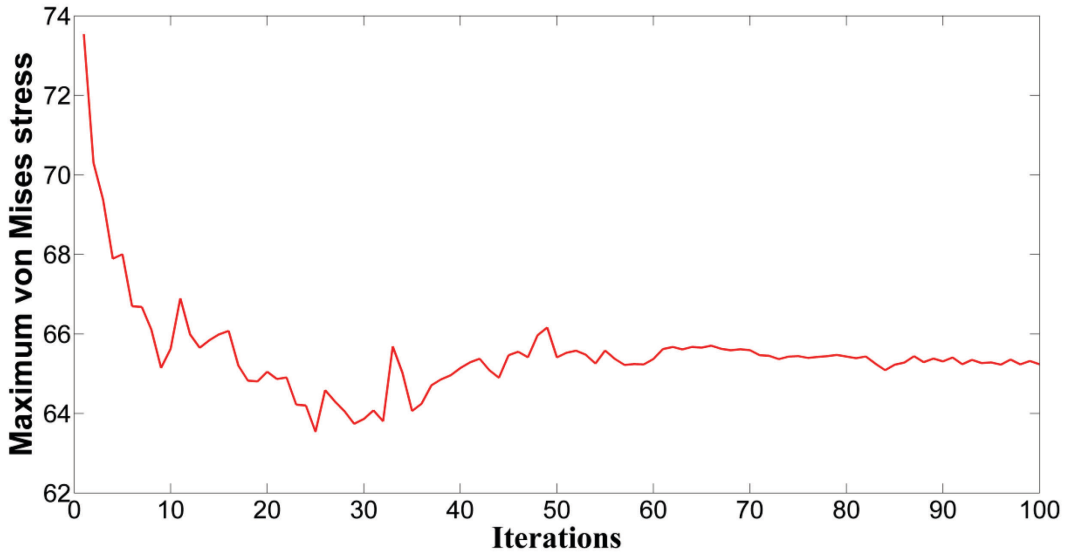


(b) maximum von Mises stress

**Figure 16** Convergence history of the L-bracket stress minimization case

A more straightforward comparison is presented in Fig. 17 to illustrate the achieved stress minimization of the 4-layer L-bracket. As shown in Fig. 17(a), before optimization, stress concentration can be observed near the boundary area of the bottom layer, namely region (A) – (E). The von Mises stress values of these elements are all high (around 73). After scanning path optimization, stress concentration in these areas is mitigated by reducing the von Mises stress to around 65. The proposed stress minimization algorithm is able to effectively prevent build failure, which is significantly beneficial for real manufacturing.

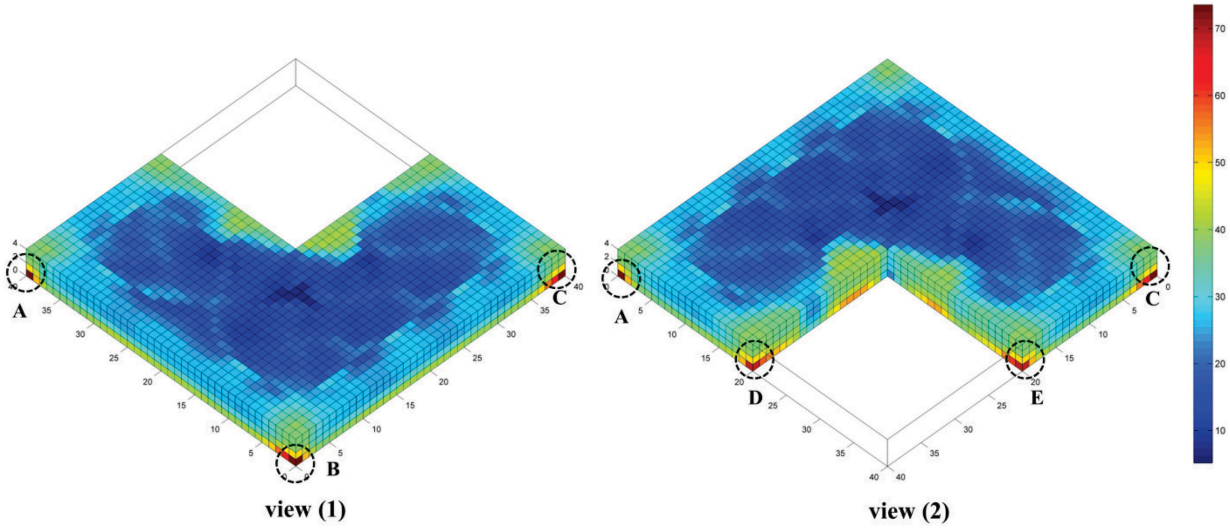


(a)

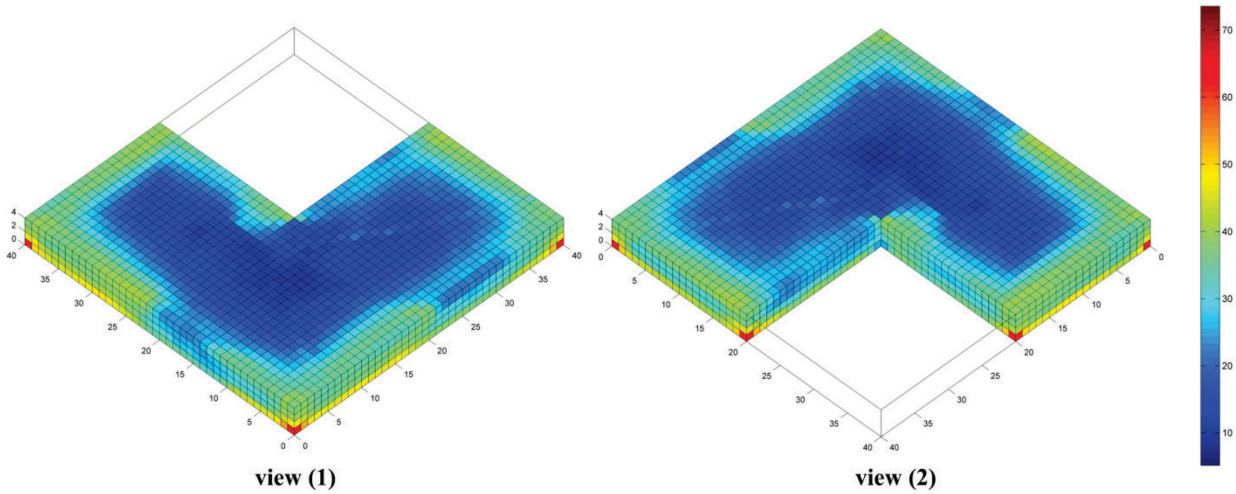


(b)

**Figure 17** Comparison of stress distribution (a) before and (b) after optimization

The layer-wise stress profile before and after optimization is studied as well. We observe little changes of the whole stress profile but at the corners and edges of the first two layers, the stress magnitude has been significantly altered as shown in Fig. 18. The maximum von Mises stress is reduced by 11.3% for the first layer and 7.20% for the second layer through optimizing the laser scanning path. The maximum stress values for the last two layers are very close in magnitude before and after optimization since they do not contribute majorly in the p-norm function in Eq. (16).

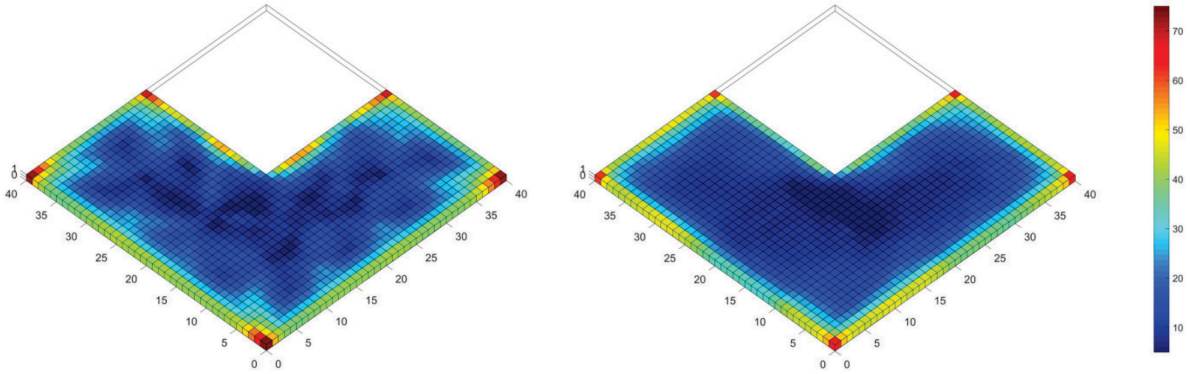


(a) Layer 1

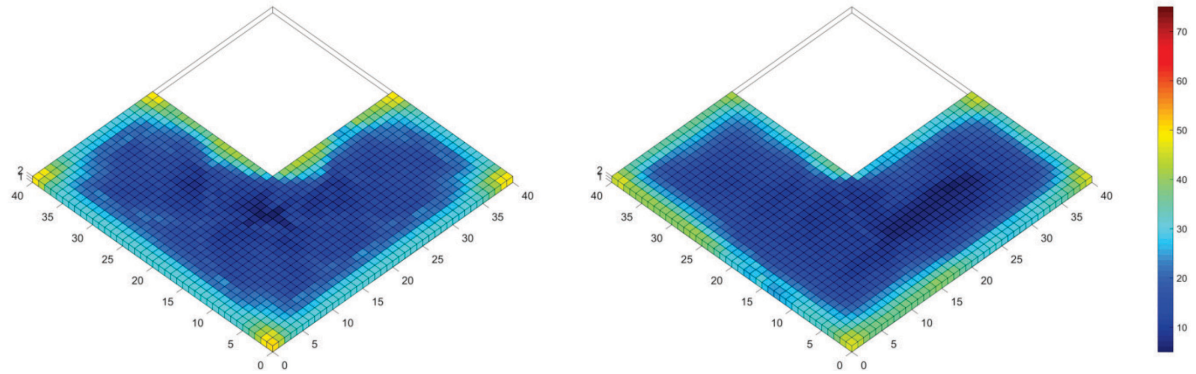

before optimization
layer-wise maximum von Mises stress: 50.02

after optimization
layer-wise maximum von Mises stress: 46.42

(b) Layer 2

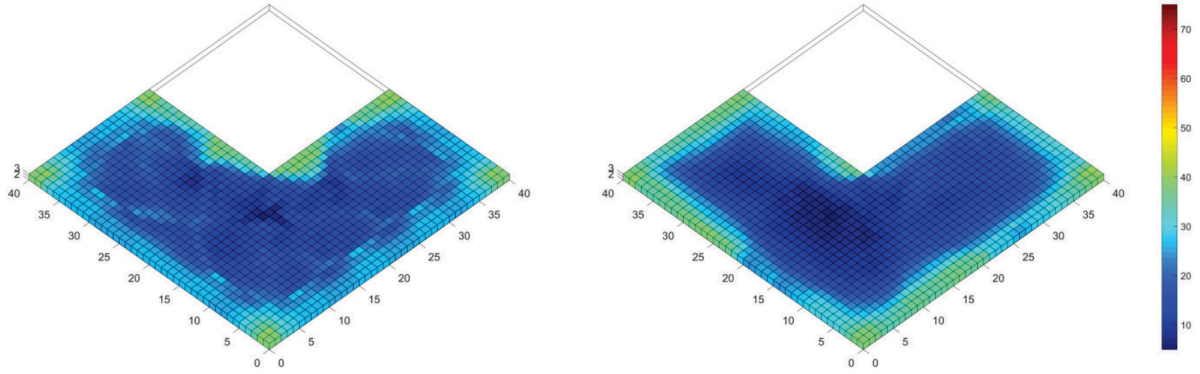

before optimization
layer-wise maximum von Mises stress: 39.76

after optimization
layer-wise maximum von Mises stress: 40.22

(c) Layer 3

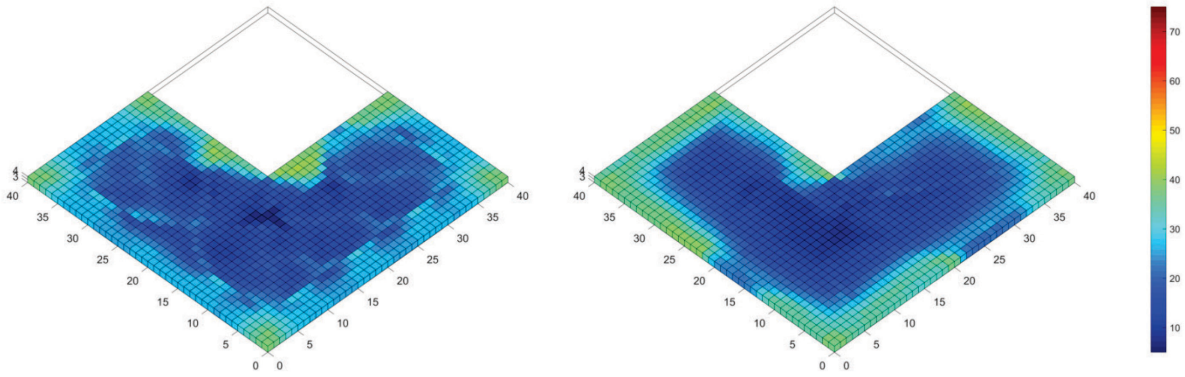

before optimization
layer-wise maximum von Mises stress: 41.15

after optimization
layer-wise maximum von Mises stress: 40.28

(d) Layer 4

**Figure 18** Layer-wise stress comparison before and after optimization

Case 5: Another case of stress minimization is performed on the 4-layer block with internal holes. The same geometry and initial scanning path as the compliance minimization case is adopted, as shown in Fig. 6. Then the optimized laser scanning path is shown in Fig. 19. Convergence histories of both the p-norm stress and maximum von Mises stress are summarized in Fig. 20, wherein the p-norm stress decreases from 78.0 to 71.7 in 100 iterations. Because of the non-linearity and localized behavior, the maximum von Mises stress oscillates and decreases from the initial value 67.6 to 61.2.

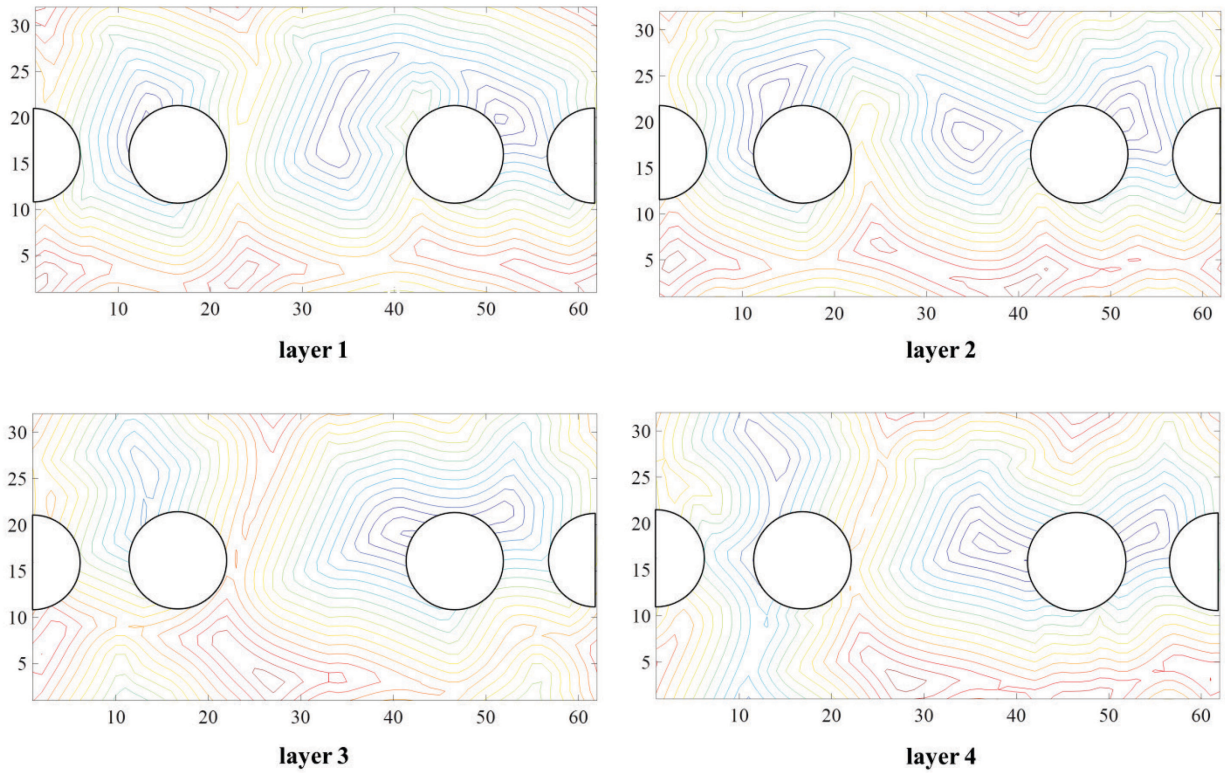


**Figure 19** Layer-wise scanning path after optimization for the block case

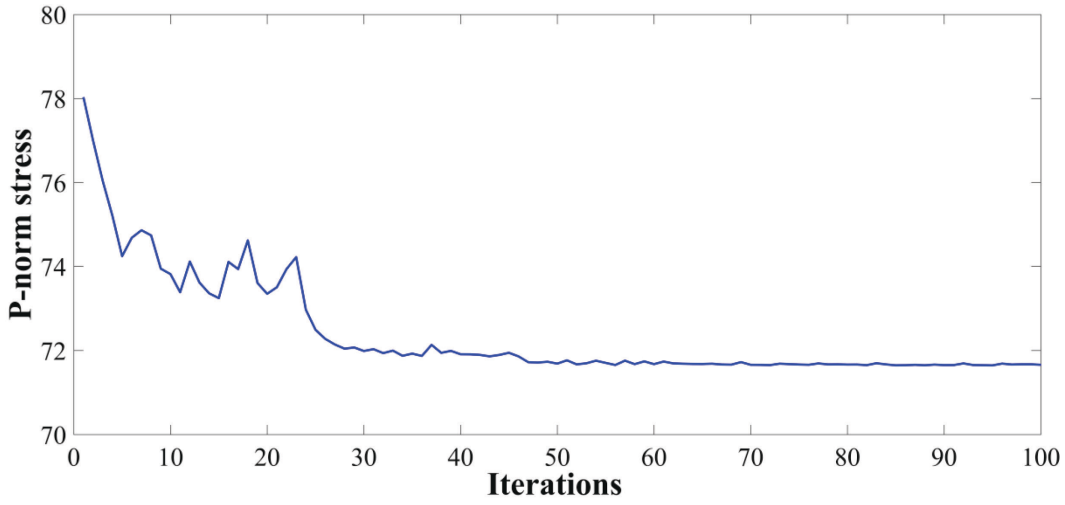


(a) p-norm stress

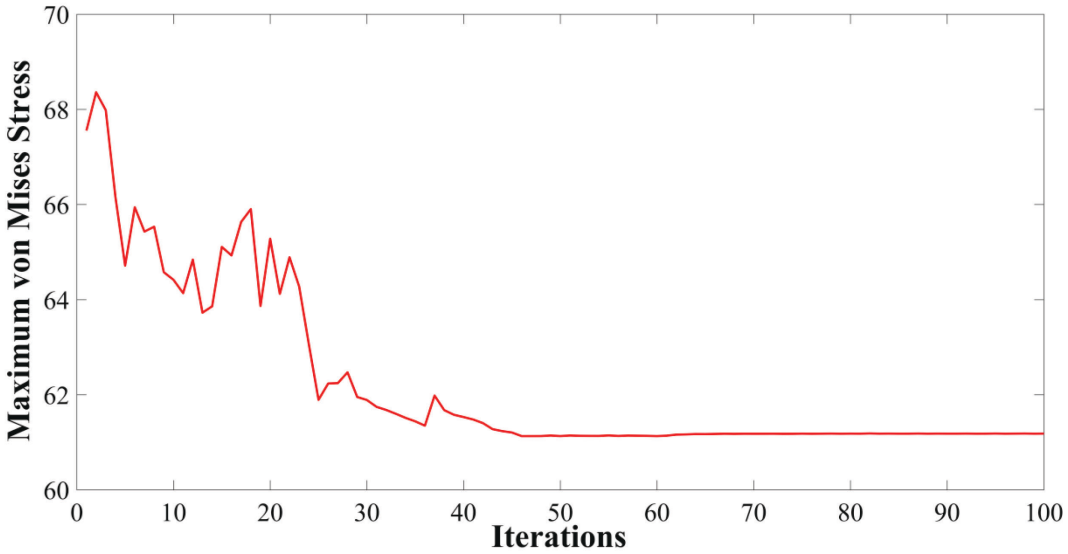


(b) maximum von Mises stress

**Figure 20** Convergence history of the block with internal holes stress minimization case

Comparison of the stress distribution before and after optimization is shown in Fig. 21. It can be seen that the stress concentration along the block edges has been evidently mitigated, and we can visibly observe the global stress reduction. Therefore, the effectiveness of scanning path optimization for stress minimization is proved in this case.

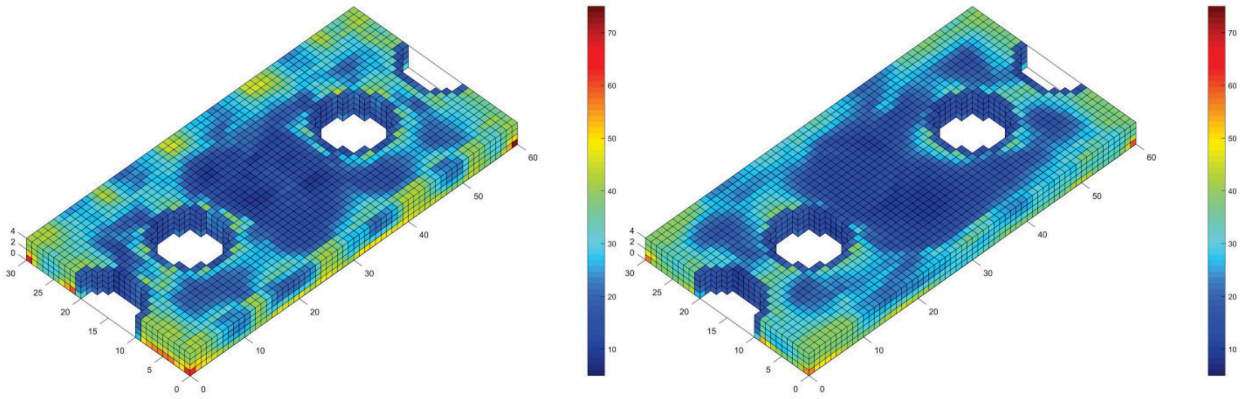

(a) (b)

**Figure 21** Comparison of stress distribution (a) before and (b) after optimization

# 6. Concurrent design

## 6.1 Stress minimization

In this section, scanning path and structural shape optimization are performed concurrently to further mitigate the stress concentration. Specifically, different level set functions are employed to represent the scanning path and structural shape separately. And the concurrent stress minimization optimization can be formulated as:

$$\begin{aligned} min.\,\sigma_{PN} &= \left[\sum_{k=1}^{n}\int_{D_k}\sigma_{von}^{P}\,H(\phi^{geo,k})d\Omega\right]^{\frac{1}{P}} \\ s.t.\,a(\mathbf{u},\mathbf{v},\boldsymbol{\Phi}^{\mathbf{geo}}) &= l(\mathbf{v},\boldsymbol{\Phi}^{\mathbf{geo}}),\quad \forall\mathbf{v}\in\mathbf{U_{ad}} \\ \underline{V}-\sum_{k=1}^{n}\int_{D_k}H(\phi^{geo,k})d\Omega &\le 0 \end{aligned} \tag{22}$$

where $\underline{V}$ is the lower bound volume ratio in structural optimization.

The Lagrangian is constructed as shown in Eq. (23), in which $\mathbf{w}$ is the adjoint variable obtained by solving Eq. (19),

$$L=\sigma_{PN}+\,a(\mathbf{u},\mathbf{w},\boldsymbol{\Phi}^{\mathbf{geo}})-l(\mathbf{w},\boldsymbol{\Phi}^{\mathbf{geo}})+\lambda\left(\underline{V}-\sum_{k=1}^{n}\int_{D_k}H(\phi^{geo,k})d\Omega\right) \tag{23}$$

The derivative of the above Lagrangian is written as:

$$\begin{aligned} L'=\frac{1}{P}\left[\sum_{k=1}^{n}\int_{D_k}\sigma_{von}^{P}\,H(\phi^{geo,k})d\Omega\right]^{\frac{1}{P}-1}\cdot\left[\sum_{k=1}^{n}\int_{D_k}P\sigma_{von}^{P-1}\,\sigma_{von}'\,H(\phi^{geo,k})d\Omega+\sum_{k=1}^{n}\int_{D_k}\sigma_{von}^{P}\,\delta(\phi^{geo,k})\cdot(\phi^{geo,k})'d\Omega\right] \\ +\sum_{k=1}^{n}\int_{D_k}\mathbf{D_k}\mathbf{e}(\mathbf{u_k'})\mathbf{e}(\mathbf{w_k})\,H(\phi^{geo,k})d\Omega+\sum_{k=1}^{n}\int_{D_k}\mathbf{D_k}\mathbf{e}(\mathbf{u_k})\boldsymbol{e}(\mathbf{w_k})\delta(\phi^{geo,k})\cdot(\phi^{geo,k})'\,d\Omega \\ -\sum_{k=1}^{n}\int_{D_k}\mathbf{D_k}\mathbf{e}\left(\mathbf{u^{in}}(\boldsymbol{\theta}^{\mathbf{k}})'\right)\mathbf{e}(\mathbf{w_k})H(\phi^{geo,k})d\Omega-\sum_{k=1}^{n}\int_{D_k}\mathbf{D_k}\mathbf{e}\left(\mathbf{u^{in}}(\boldsymbol{\theta}^{\mathbf{k}})\right)\mathbf{e}(\mathbf{w_k})\delta(\phi^{geo,k})\cdot(\phi^{geo,k})'d\Omega \\ +\lambda\sum_{k=1}^{n}\int_{D_k}\delta(\phi^{geo,k})\cdot(\phi^{geo,k})'\,d\Omega \end{aligned} \tag{24}$$

Finally, by expanding all the inherent strain derivative terms $\mathbf{e}\left(\mathbf{u^{in}}(\boldsymbol{\theta}^{\mathbf{k}})'\right)$ in the Lagrangian and collecting all the terms containing $\frac{\partial\phi_{i,j}^{scan,k}}{\partial t}$ and $\delta(\phi^{geo,k})\cdot(\phi^{geo,k})'$, the sensitivity results of level set functions representing scanning path and geometry are obtained, respectively. The normal update velocity of scanning path level set function $V_{N\,i,j}^{scan,k}$ in the concurrent design is the same as Eq. (20), and the structure boundary update velocity in iterations is derived as:

$$V_N^{geo,k} = \frac{1}{P}\left[\sum_{k=1}^{n}\int_{D_k}\sigma_{von}^{P}\,H\left(\phi^{geo,k}\right)d\Omega\right]^{\frac{1}{P}-1}\cdot\sigma_{von}^{P} + \mathbf{D_k e(u_k) e(w_k)} + \mathbf{D_k e}\left(\mathbf{u^{in}}\left(\boldsymbol{\theta}^{\mathbf{k}}\right)\right)\mathbf{e}((\mathbf{w_k}) + \boldsymbol{\lambda} \tag{25}$$

The volume constraint is addressed using the Augmented Lagrange multiplier method, which adjusts the Lagrange multiplier in iterations:

$$\lambda_{n+1} = \lambda_n + \mu_n\left(\underline{V} - \sum_{k=1}^{n}\int_{D_k} H(\phi^{geo,k})d\Omega\right) \tag{26}$$

$$\mu_{n+1} = \alpha\mu_n \text{ where } 0 < \alpha < 1 \tag{27}$$

in which $\mu$ is the penalization factor and $\alpha$ is the adjustment parameter.

Case 6: Concurrent scanning path and structural optimization for the four-layer L bracket is explored. The initial structure and scanning path for the concurrent optimization are shown in Fig. 2. The objective is to minimize residual stress under the minimum material volume ratio of 0.9. We still assume the materials have a Young's modulus of 2,100 for solid and $10^{-3}$ for the void.

The optimization result is shown in Fig. 22. Under the constraint of minimum material volume of 0.9, the L-bracket outline becomes smoother than the previous structure with five 90° corners as a result of shape optimization. This optimized L-bracket has a maximum residual stress of 55, which is much smaller than the 65 for the scanning path-only optimization.

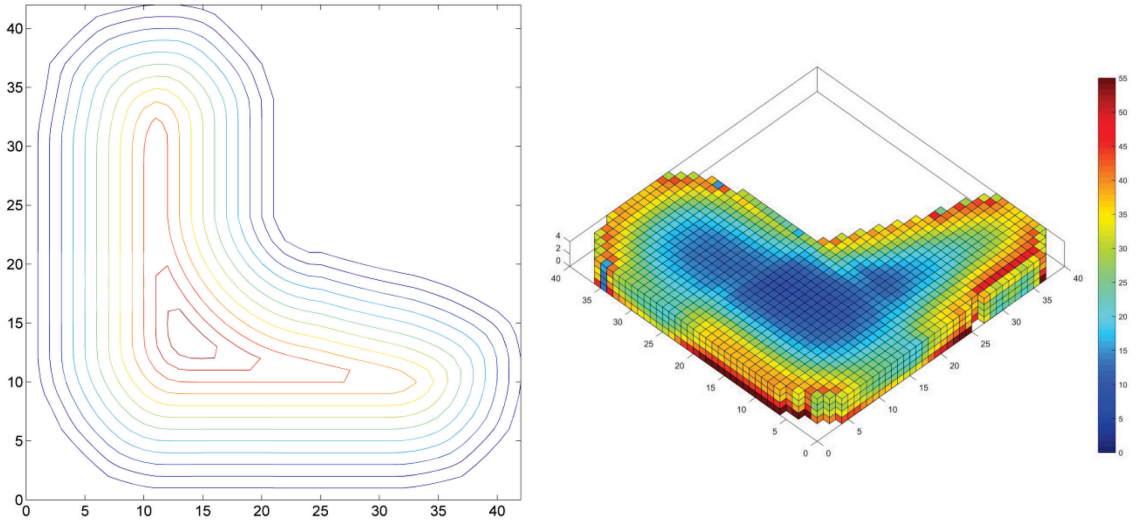

(a) (b)

**Figure 22** (a) Optimized structure and (b) bottom layer stress distribution

Layer-wise scanning path is simultaneously optimized according to the derived velocities in Eq. (19). The optimized scanning path is summarized in Fig. 23. The convergence history for the concurrent design is demonstrated in Fig. 24. The p-norm stress decreases from 99.2 to 91 in

100 iterations while the volume ratio drops to the lower limit of 0.9. The maximum von Mises stress decreases to 55.5. Compared with Case 3, where only the layer-wise scanning path of L-bracket is optimized, we can find that the scanning patterns in Case 6 are highly different while the concurrent design has a lower maximum stress after optimization. A reasonable explanation is that the concurrent optimization has a larger design space consisting of both scanning path and geometry. It can be found that the stress concentration occurs at the corners of the L-bracket after scanning path optimization in Case 3, while in this concurrent design, all the corners with stress concentration vanish after shape optimization and the maximum stress occurs on the edge of the optimized shape as shown in Fig. 22(b).

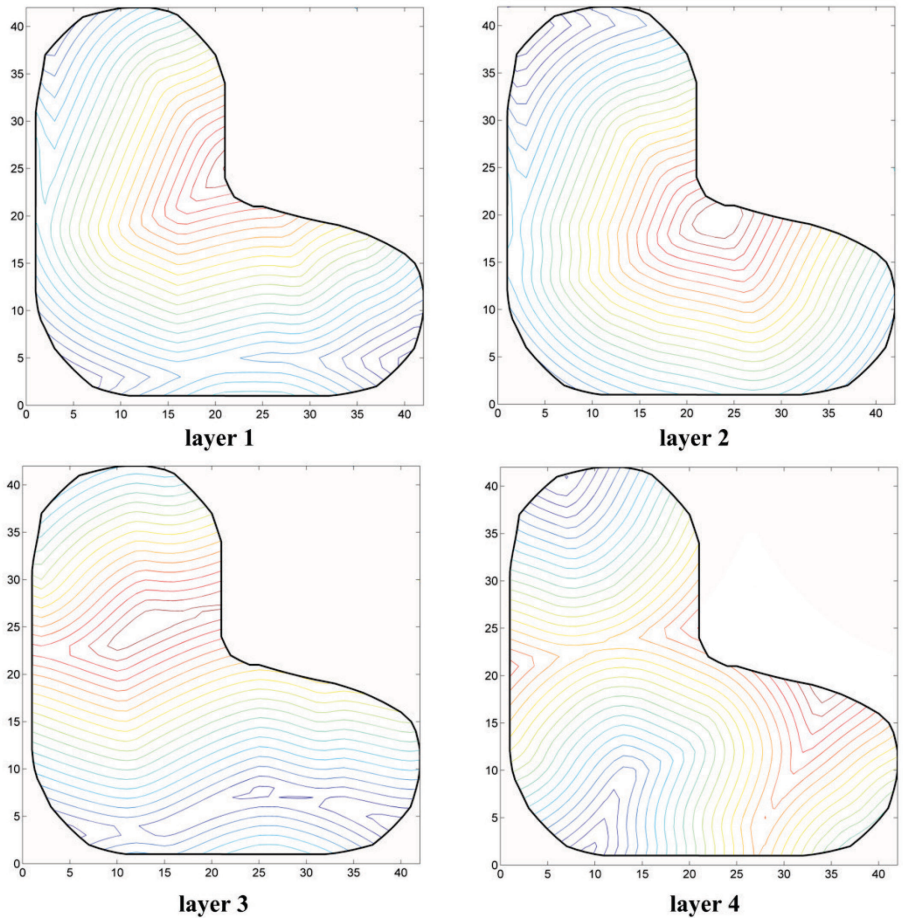


**Figure 23** Layer-wise scanning path after optimization

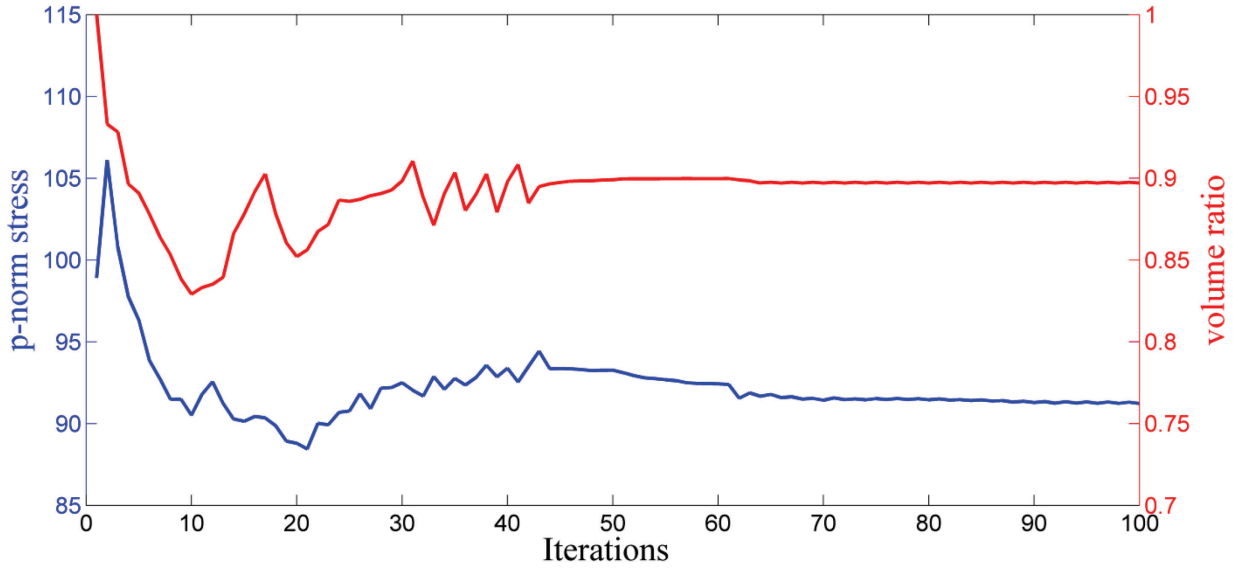


(a)

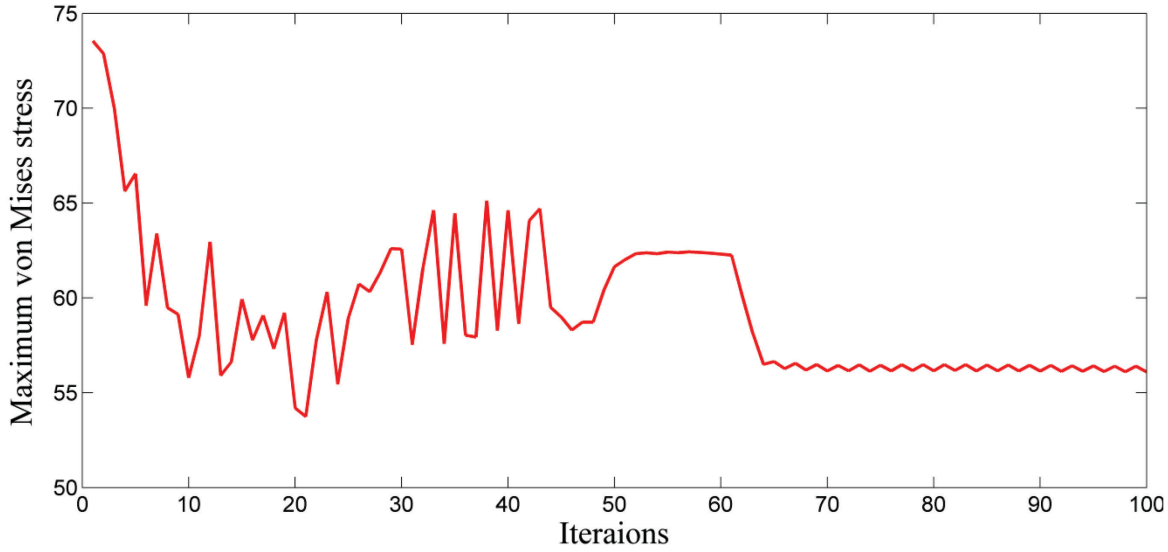


(b)

**Figure 24** Convergence history of the concurrent design

### 6.2 Compliance minimization

Another concurrent design problem is the compliance minimization in which the topology and scanning path are optimized. The problem is formulated as:

$$\min. \quad J = \sum_{k=1}^{N} \left[ \int_{D_k} D_k e(u_k) e(u_k) H\left(\phi^{geo,k}\right) d\Omega \right] \tag{28}$$

$$s.t.\, a(u, v, \Phi^{geo}) = l(v, \Phi^{geo}), \quad \forall v \in U_{ad}$$

$$\sum_{k=1}^{n} \int_{D_k} H\left(\phi^{geo,k}\right) d\Omega - \overline{V} \leq 0$$

where $\overline{V}$ the upper bound volume ratio in structural optimization.

The Lagrangian is formulated as:

$$L = J + a(u, w, \Phi^{geo}) - l(w, \Phi^{geo}) + \lambda \left( \sum_{k=1}^{n} \int_{D_k} H(\phi^{geo,k}) d\Omega - \overline{V} \right) \quad (29)$$

By taking derivative of the Lagrangian, the sensitivity to update scanning path level set field can be obtained by Eq. (15) and the structure boundary update velocity is:

$$V_N^{geo,k} = -D_k e(u_k) e(u_k) + 2 D_k e\left(u^{in}(\theta^k)\right) e(u_k) + \lambda \quad (30)$$

Case 7: In this case, the cantilever beam with a volume ratio of 0.5 after compliance minimization is taken as the initial design for concurrent optimization, as shown in Fig. 25(a). The initial cantilever beam consists of four layers with the same geometry and its volume ratio is set to be 1.0 in concurrent design. The initial scanning path for each layer is shown in Fig. 26(a). Three concurrent optimizations are performed where the cantilever beam geometry and layer-wise scanning are optimized for compliance reduction simultaneously under different volume ratio of 0.95, 0.90 and 0.85, respectively. The optimized structures under different volume constraints are shown in Fig. 25(b)-(d). It can be found that structure with lower volume ratio has a smaller value of compliance because the reduction in structure volume leads to less thermal loading.

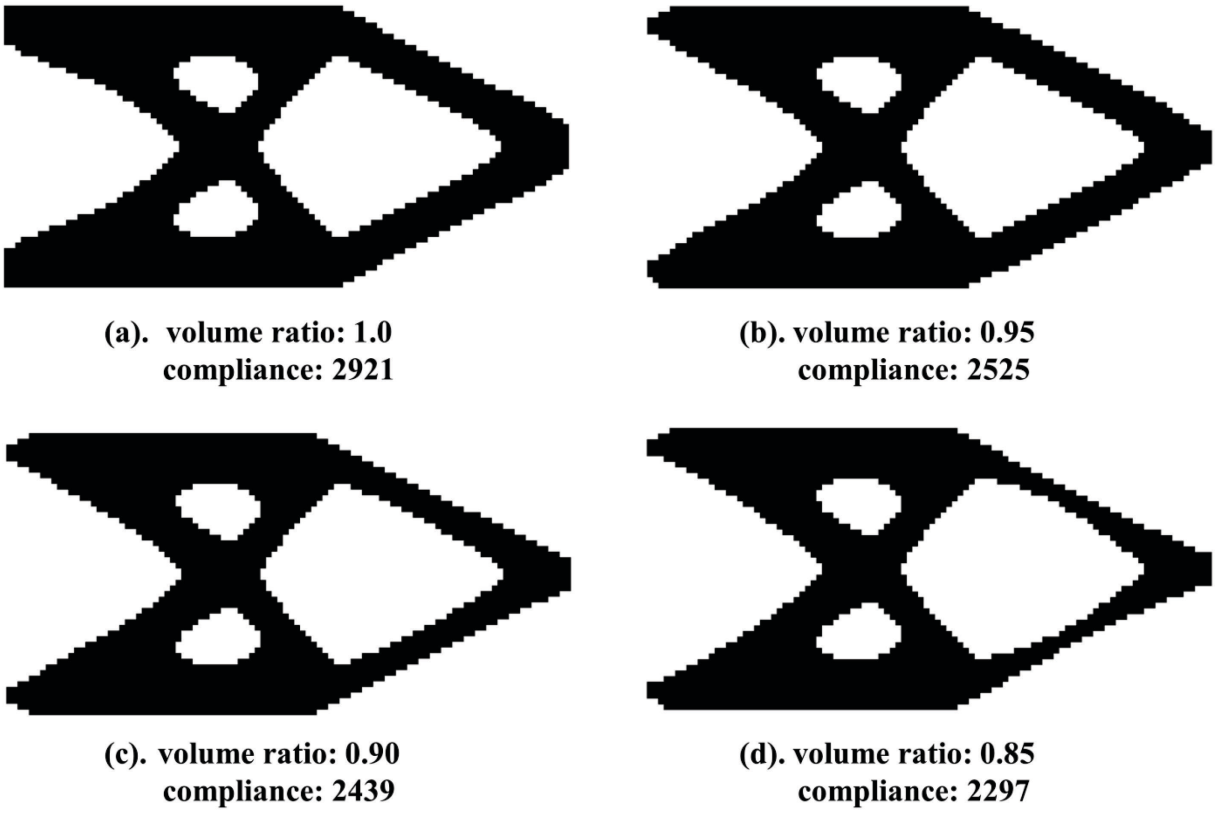


**Figure 25** Cantilever beam before and after optimization

All the three concurrent optimizations converge in 100 iterations. The initial scanning path is shown in Fig. 26(a) and optimized scanning paths of the bottom layer under volume ratio of 0.95, 0.90 and 0.85 are shown in Fig. 26(b)-(d). The optimized scanning paths under volume ratio of 0.95, 0.9 and 0.85 are nearly identical because of the highly similar structures.

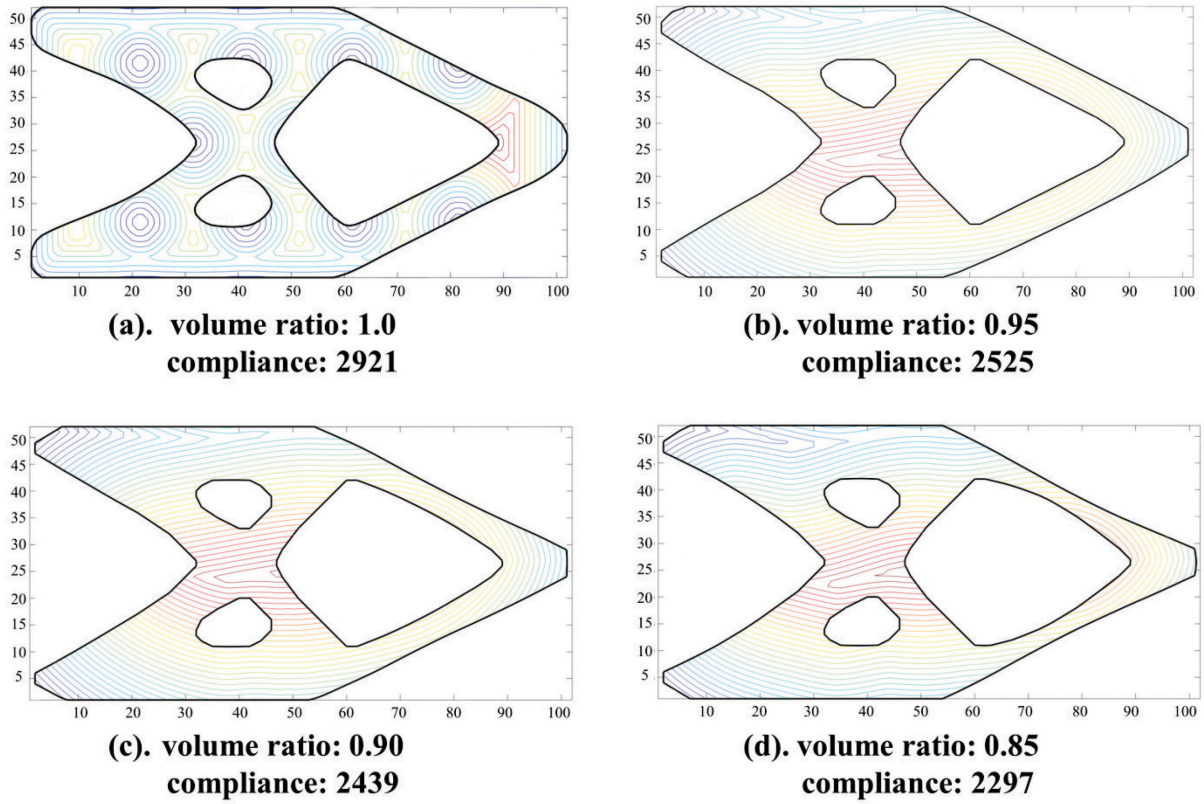


**Figure 26** Initial and optimized scanning path of the bottom layer

## 7. Conclusion

This paper proposes a continuous laser scanning path optimization method for metal additive manufacturing process including powder bed fusion, wire-feed and directed energy deposition. The individual level contours are employed as scanning paths of which the continuity and equal hatching space are ensured, and the relevant thermal loading is calculated from scanning orientation dependent inherent strain vectors. A novel adaptive level set adjustment (ALSA) strategy is developed to address the instability issue caused by ignoring the non-implementable sensitivities, i.e., preventing zero level set contours from over-shrinking/expanding. The numerical examples exhibit the effectiveness of this proposed optimization method in mitigating stress concentration and compliance minimization, while the constant hatching space among scanning lines are always guaranteed owing to the signed distance feature of the level set function.

More importantly, this scanning path optimization method exhibits the scalability to much taller and complex structures consisting of multiple layers and features such as overhang, and the ability to extend to concurrent design that takes both topology optimization and laser scanning path planning into account. We have found that, in the L-bracket stress minimization problem, concurrent design has a smaller maximum von Mises stress than only optimizing scanning path because of a larger design space consists of both structure and scanning path.

For future work, further scalability to scanning path optimization of real AM parts with thousands of layers can be expected by leveraging the GPU-based finite element analysis. Another important issue to address is the gaps between contours that can lead to lack of fusion and porosities. Therefore, improvements for this algorithm to ensure gap-free scanning path will be investigated.

## Acknowledgement

Financial support from National Science Foundation (CMMI-1634261) is gratefully acknowledged.

## Reference

[1] S. Clijsters, T. Craeghs, J.-P. Kruth, A priori process parameter adjustment for SLM process optimization, in: Innovative developments on virtual and physical prototyping, Taylor & Francis Group., 2012, pp. 553-560.

[2] R. Mertens, S. Clijsters, K. Kempen, J.-P. Kruth, Optimization of scan strategies in selective laser melting of aluminum parts with downfacing areas, Journal of Manufacturing Science and Engineering, 136 (2014) 061012.

[3] J.-P. Kruth, J. Deckers, E. Yasa, R. Wauthlé, Assessing and comparing influencing factors of residual stresses in selective laser melting using a novel analysis method, Proceedings of the institution of mechanical engineers, Part B: Journal of Engineering Manufacture, 226 (2012) 980-991.

[4] Y. Lu, S. Wu, Y. Gan, T. Huang, C. Yang, L. Junjie, J. Lin, Study on the microstructure, mechanical property and residual stress of SLM Inconel-718 alloy manufactured by differing island scanning strategy, Optics & Laser Technology, 75 (2015) 197-206.

[5] K. Dai, L. Shaw, Distortion minimization of laser-processed components through control of laser scanning patterns, Rapid Prototyping Journal, 8 (2002) 270-276.

[6] E.R. Denlinger, M. Gouge, J. Irwin, P. Michaleris, Thermomechanical model development and in situ experimental validation of the Laser Powder-Bed Fusion process, Additive Manufacturing, 16 (2017) 73-80.

[7] S.S. Bo Cheng, Kevin Chou, Stress and deformation evaluations of scanning strategy effect in selective laser melting, Additive Manufacturing, (2017).

[8] E. Foroozmehr, R. Kovacevic, Effect of path planning on the laser powder deposition process: thermal and structural evaluation, The International Journal of Advanced Manufacturing Technology, 51 (2010) 659-669.

[9] L.H. Ahmed Hussein, Chunze Yan, Richard Everson, Finite element simulation of the temperature and stress fields in single layers built without-support in selective laser melting, Materials and Design, (2013).

[10] D. Ding, Z.S. Pan, D. Cuiuri, H. Li, A tool-path generation strategy for wire and arc additive manufacturing, The international journal of advanced manufacturing technology, 73 (2014) 173-183.

[11] B.E. Carroll, T.A. Palmer, A.M. Beese, Anisotropic tensile behavior of Ti–6Al–4V components fabricated with directed energy deposition additive manufacturing, Acta Materialia, 87 (2015) 309-320.

[12] D. Ding, Z. Pan, D. Cuiuri, H. Li, A practical path planning methodology for wire and arc additive manufacturing of thin-walled structures, Robotics and Computer-Integrated Manufacturing, 34 (2015) 8-19.

[13] D. Ding, Z. Pan, D. Cuiuri, H. Li, S. van Duin, N. Larkin, Bead modelling and implementation of adaptive MAT path in wire and arc additive manufacturing, Robotics and Computer-Integrated Manufacturing, 39 (2016) 32-42.

[14] R. Ponche, O. Kerbrat, P. Mognol, J.-Y. Hascoet, A novel methodology of design for Additive Manufacturing applied to Additive Laser Manufacturing process, Robotics and Computer-Integrated Manufacturing, 30 (2014) 389-398.

[15] D.E. Smith, R. Hoglund, Continuous fiber angle topology optimization for polymer fused fillament fabrication, in: Annu. Int. Solid Free. Fabr. Symp. Austin, TX, 2016.

[16] J. Liu, J. Liu, H. Yu, H. Yu, Concurrent deposition path planning and structural topology optimization for additive manufacturing, Rapid Prototyping Journal, 23 (2017) 930-942.

[17] Q. Xia, T. Shi, Optimization of composite structures with continuous spatial variation of fiber angle through Shepard interpolation, Composite Structures, 182 (2017) 273-282.

[18] C. Kiyono, E. Silva, J. Reddy, A novel fiber optimization method based on normal distribution function with continuously varying fiber path, Composite Structures, 160 (2017) 503-515.

[19] C.J. Brampton, K.C. Wu, H.A. Kim, New optimization method for steered fiber composites using the level set method, Structural and Multidisciplinary Optimization, 52 (2015) 493-505.

[20] J. Liu, A.C. To, Deposition path planning-integrated structural topology optimization for 3D additive manufacturing subject to self-support constraint, Computer-Aided Design, 91 (2017) 27-45.

[21] H. Shen, J. Fu, Z. Chen, Y. Fan, Generation of offset surface for tool path in NC machining through level set methods, The International Journal of Advanced Manufacturing Technology, 46 (2010) 1043-1047.

[22] C. Zhuang, Z. Xiong, H. Ding, High speed machining tool path generation for pockets using level sets, International Journal of Production Research, 48 (2010) 5749-5766.

[23] P. Zhang, J. Liu, A.C. To, Role of anisotropic properties on topology optimization of additive manufactured load bearing structures, Scripta Materialia, 135 (2017) 148-152.

[24] X. Liang, Q. Chen, L. Cheng, Q. Yang, A. To, A modified inherent strain method for fast prediction of residual deformation in additive manufacturing of metal parts, in: 2017 Solid Freeform Fabrication Symposium Proceedings, Austin, Texas, 2017.

[25] Q. Chen, X. Liang, D. Hayduke, J. Liu, L. Cheng, J. Oskin, R. Whitmore, A.C. To, An inherent strain based multiscale modeling framework for simulating part-scale residual deformation for direct metal laser sintering, Additive Manufacturing, 28 (2019) 406-418.

[26] K. Dai, L. Shaw, Thermal and stress modeling of multi-material laser processing, Acta Materialia, 49 (2001) 4171-4181.

[27] C. Fu, Y. Guo, Three-dimensional temperature gradient mechanism in selective laser melting of Ti-6Al-4V, Journal of Manufacturing Science and Engineering, 136 (2014) 061004.

[28] P. Prabhakar, W.J. Sames, R. Dehoff, S.S. Babu, Computational modeling of residual stress formation during the electron beam melting process for Inconel 718, Additive Manufacturing, 7 (2015) 83-91.

[29] E.R. Denlinger, J. Irwin, P. Michaleris, Thermomechanical Modeling of Additive Manufacturing Large Parts, Journal of Manufacturing Science and Engineering, 136 (2014) 061007.

[30] Y. Ueda, K. Fukuda, K. Nakacho, S. Endo, A new measuring method of residual stresses with the aid of finite element method and reliability of estimated values, Journal of the Society of Naval Architects of Japan, 1975 (1975) 499-507.

[31] M.R. Hill, D.V. Nelson, The inherent strain method for residual stress determination and its application to a long welded joint, ASME-PUBLICATIONS-PVP, 318 (1995) 343-352.

[32] H. Murakawa, Y. Luo, Y. Ueda, Prediction of welding deformation and residual stress by elastic FEM based on inherent strain, Journal of the society of Naval Architects of Japan, 1996 (1996) 739-751.

[33] M. Yuan, Y. Ueda, Prediction of residual stresses in welded T-and I-joints using inherent strains, Journal of Engineering Materials and Technology, Transactions of the ASME, 118 (1996) 229-234.

[34] L. Zhang, P. Michaleris, P. Marugabandhu, Evaluation of applied plastic strain methods for welding distortion prediction, Journal of Manufacturing Science and Engineering, 129 (2007) 1000-1010.

[35] X. Liang, L. Cheng, Q. Chen, Q. Yang, A. To, A Modified Method for Estimating Inherent Strains from Detailed Process Simulation for Fast Residual Distortion Prediction of Single-Walled Structures Fabricated by Directed Energy Deposition, Additive Manufacturing, 23 (2018) 471-486.

[36] N. Keller, V. Ploshikhin, New method for fast predictions of residual stress and distortion of AM parts, in: Solid Freeform Fabrication Symposium, Austin, Texas, 2014, pp. 1229-1237.

[37] M. Bugatti, Q. Semeraro, Limitations of the Inherent Strain Method in Simulating Powder Bed Fusion Processes, Additive Manufacturing, 23 (2018) 329-346.

[38] L. Cheng, X. Liang, J. Bai, Q. Chen, J. Lemon, A. To, On Utilizing Topology Optimization to Design Support Structure to Prevent Residual Stress Induced Build Failure in Laser Powder Bed Metal Additive Manufacturing, Additive Manufacturing, (2019).

[39] S. Osher, J.A. Sethian, Fronts propagating with curvature-dependent speed: algorithms based on Hamilton-Jacobi formulations, Journal of computational physics, 79 (1988) 12-49.

[40] M.Y. Wang, X. Wang, D. Guo, A level set method for structural topology optimization, Computer methods in applied mechanics and engineering, 192 (2003) 227-246.

[41] G. Allaire, F. Jouve, A.-M. Toader, Structural optimization using sensitivity analysis and a level-set method, Journal of computational physics, 194 (2004) 363-393.

[42] Y. Wang, Z. Luo, Z. Kang, N. Zhang, A multi-material level set-based topology and shape optimization method, Computer Methods in Applied Mechanics and Engineering, 283 (2015) 1570-1586.

[43] P. Dunning, C. Brampton, H. Kim, Simultaneous optimisation of structural topology and material grading using level set method, Materials Science and Technology, 31 (2015) 884-894.

[44] P. Liu, Y. Luo, Z. Kang, Multi-material topology optimization considering interface behavior via XFEM and level set method, Computer methods in applied mechanics and engineering, 308 (2016) 113-133.

[45] J. Liu, Q. Chen, Y. Zheng, R. Ahmad, J. Tang, Y. Ma, Level set-based heterogeneous object modeling and optimization, Computer-Aided Design, (2019).

[46] J. Liu, Q. Chen, X. Liang, A.C. To, Manufacturing cost constrained topology optimization for additive manufacturing, Frontiers of Mechanical Engineering, 14 (2019) 213-221.

[47] Z. Kang, Y. Wang, Integrated topology optimization with embedded movable holes based on combined description by material density and level sets, Computer methods in applied mechanics and engineering, 255 (2013) 1-13.

[48] P.D. Dunning, H. Alicia Kim, A new hole insertion method for level set based structural topology optimization, International Journal for Numerical Methods in Engineering, 93 (2013) 118-134.

[49] J.A. Sethian, A fast marching level set method for monotonically advancing fronts, Proceedings of the National Academy of Sciences, 93 (1996) 1591-1595.

[50] J.A. Sethian, Level set methods and fast marching methods: evolving interfaces in computational geometry, fluid mechanics, computer vision, and materials science, Cambridge university press, 1999.

[51] C. Le, J. Norato, T. Bruns, C. Ha, D. Tortorelli, Stress-based topology optimization for continua, Structural and Multidisciplinary Optimization, 41 (2010) 605-620.

[52] A. Takezawa, G.H. Yoon, S.H. Jeong, M. Kobashi, M. Kitamura, Structural topology optimization with strength and heat conduction constraints, Computer Methods in Applied Mechanics and Engineering, 276 (2014) 341-361.